Utilizing Synchrotron Radiation for the Characterization of Biodegradable Magnesium Alloys — From Alloy Development to the Application as Implant Material

Zeller-Plumhoff, Berit; Tolnai, Domonkos; Wolff, Martin; Greving, Imke; Hort, Norbert; Willumeit-Römer, Regine

Utilizing Synchrotron Radiation for the Characterization of Biodegradable Magnesium Alloys—From Alloy Development to the Application as Implant Material

Berit Zeller-Plumhoff,* Domonkos Tolnai, Martin Wolff, Imke Greving, Norbert Hort, and Regine Willumeit-Römer

Magnesium alloys are highly attractive for their application as structural materials as well as medical implants. A range of alloying systems exists which are investigated, e.g., in terms of alloy microstructure changes, in particular during different processing steps or mechanical testing, and in terms of the associated corrosion performance of the material. Synchrotron radiation and in particular synchrotron radiation microcomputed tomography and nanotomography yield a unique opportunity to investigate such changes and processes in 3D at high resolution and in situ, thus significantly broadening our knowledge base. Herein, the benefits of using synchrotron radiation for the investigation of magnesium alloys with particular respect to its application as a biodegradable implant are demonstrated. Advances in experimental environments for in situ testing are reviewed, and all stages of materials testing are covered in which synchrotron radiation has been used, i.e., from developing and processing of the material, to corrosion testing and assessing implant integration and stability ex vivo. This review incorporates advances both in micro- and nanotomographic imaging regimes and further includes complementary techniques, such as X-ray diffraction, small angle X-ray scattering, X-ray fluorescence, and diffraction tomography. Finally, an outlook into future developments is provided.

1. Introduction

Magnesium (Mg)-based alloys are investigated for the use as lightweight structural metals, e.g., in the automotive industry,[1]

Dr. B. Zeller-Plumhoff, Dr. D. Tolnai, M. Wolff, Dr. N. Hort,
Dr. R. Willumeit-Römer
Institute of Metallic Biomaterials
Helmholtz-Zentrum Hereon GmbH
Max-Planck-Str. 1, Geesthacht 21502, Germany
E-mail: berit.zeller-plumhoff@hereon.de

Dr. I. Greving
Institute of Materials Physics
Helmholtz-Zentrum Hereon GmbH
Max-Planck-Str. 1, Geesthacht 21502, Germany

The ORCID identification number(s) for the author(s) of this article can be found under https://doi.org/10.1002/adem.202100197.

as biodegradable implant materials[2] and for hydrogen storage.[3] The choice of alloying system and subsequent processing of the material is a crucial factor for the degradation profile of the alloy and its mechanical properties.[4–7] This review focuses on use of Mg alloys as implant material, with some references to its application as a structural metal.

The degradation profile of Mg alloys is of particular importance for their application as implant materials, as a controlled degradation is required to ensure cell viability and implant stability in vivo.[8,9] During the development of Mg alloys for the application as a biodegradable implant, alloying systems are carefully selected and manufactured, with their microstructure being tailored according to specifications by selecting the appropriate processing route. The microstructure and the mechanical properties of the alloy will be evaluated and the alloy is then tested for in vitro degradation in an aqueous environment under physiological conditions (pH $\approx$7.4, 37 °C, 5% CO_2, 21% O_2, 95% rel. humidity) with and without cells to assess its general degradation properties and cell viability.[10] The mechanical properties and degradation profile need to be tailored depending on the application of the implant. Mg alloys for bone support, for example, require mechanical properties close to that of bone. For bone, the average Young's modulus is between 7 and 31 GPa, depending on the type of bone and its hydration state.[11,12] In longitudinal direction, the bone's tensile and compressive ultimate strength have been reported to be between 93 and 135 MPa, and 154 and 205 MPa, respectively.[13,14] Finally, the elongation to failure of the clinically approved MAGNEZIX screw by Syntellix AG (Hanover, Germany) was determined to be 8%.[15] By contrast, Mg alloys designed for the use as stents must possess a minimum ultimate tensile strength of 300 MPa, low yield strength of 200–300 MPa, and higher ductility (min. 15%–18% elongation to failure, preferably 30%) for their successful deployment.[16,17] Finally, in vivo animal experiments are conducted to evaluate the alloy suitability for the translation into the clinic.

During all stages of implant development, morphological and structural analyses are conducted, e.g., to evaluate the present

phases or the integration of the implant into the target tissue. The control of these different stages depends on the level of understanding of the underlying biological and physical processes. Synchrotron radiation (SR)-based techniques, in particular imaging and scattering techniques, provide a powerful tool to enhance this understanding by enabling in situ testing of the material. In this review, we are detailing the opportunities that SR-based techniques provide for the characterization of Mg alloys in terms of alloy development, in vitro testing, and finally their behavior in bone by ex vivo analysis. To date, no Mg-based stents have been investigated ex vivo using SR. The review is divided into three corresponding sections, each of which will detail the use of imaging techniques and complementary analysis methods. Initially, we will introduce the concept of a synchrotron briefly, as well as the relevant characterization methods.

2. Synchrotron Techniques for Materials Characterization

Synchrotron sources are accelerators in which either electrons or positrons are used to generate X-ray radiation by changing the particles' direction, either in bending magnets or in insertion devices.[18] The generated radiation is guided toward different beamlines, each of which is dedicated to one or few experiment types. In contrast to laboratory X-ray sources, synchrotron sources provide greater brilliance and coherence. A source's brilliance quantifies the number of photons emitted per second with respect to the beam collimation (measure of spatial divergence), the source area, and the spectral distribution of the radiation[18]

$$\text{Brilliance} = \frac{\text{photons/second}}{(\text{mrad})^2(\text{mm}^2\ \text{source area})(0.1\%\ \text{energy bandwidth})}$$

(1)

Brilliance is a figure-of-merit that enables the comparison of different X-ray sources. For example, some of the most brilliant synchrotron facilities, such as the European Synchrotron Radiation Facility (ESRF) or PETRA III at Deutsches Elektronen Synchrotron (DESY), currently have a brilliance in the order of 10^{21} photons $\text{s}^{-1}/0.1\%\ \text{mm}^{-2}\ \text{mrad}^{-2}$, which is expected to be enhanced by a factor of 100 with upcoming upgrades.[19,20] By contrast, modern laboratory X-ray tubes have a brilliance of the order of 10^{10} photons $\text{s}^{-1}/0.1\%\ \text{mm}^{-2}\ \text{mrad}^{-2}$.[21] Therefore, while X-ray sources can reach similar spatial resolutions for imaging, for example, SR still enables faster imaging with similar or better image quality in terms of noise and contrast.[22] Coherence describes the spatial and chromatic deviation of the X-rays from an ideal monochromatic plane wave, which depends, for example, on the source size. High coherence is required for a number of specialized techniques available at synchrotron sources.[18]

Synchrotron radiation microcomputed tomography (SRμCT) is increasingly used for studying the material microstructure or the osseointegration of an implant due to its 3D nature and high material penetration depth. SRμCT can be based on different contrast modes; in its simplest form it is based on attenuation contrast by the samples features and relates incoming and transmitted beam intensities via the Beer–Lambert law. Features

with higher atomic numbers or density attenuate X-ray more strongly, leading to less transmission of the beam. For low-attenuating samples or those with little attenuation contrast between the sample features, phase contrast techniques can be used. In these techniques, contrast is generated based on differences in phase shift introduced by different features of the sample exhibiting different refractive indices. Phase contrast imaging generally relies on the high coherence of SR. Propagation-based phase contrast imaging (PPCI) is the simplest to implement, as it does not rely on any optical elements. PPCI is based on the interference of X-rays that are refracted by different sample features. This interference becomes stronger, the further the X-rays propagate from the sample toward the detector.

Due to the advances in SR brilliance and detector technologies, tomograms of mm-sized specimens can nowadays be obtained in the order of seconds and below while maintaining high signal-to-noise ratios and spatial resolutions of few micrometers, thus guiding the way to real-time dynamic testing of material behavior in situ.[23] The image magnification in SRμCT is given by an optical magnification of the image in the visible light regime, thus limiting the resolution of the technique to the diffraction limit of visible light, which is ≈200–250 nm. Therefore, when resolutions significantly below 1 μm are desired, nanotomographic imaging needs to be used.

Nanotomographic 3D imaging using synchrotron radiation (SRnCT) includes near-field X-ray holography (NFHT), transmission X-ray microscopy (TXM), and ptychography. NFHT is based on the generation of a cone beam by focusing the X-rays to a secondary source and the subsequent imaging of the sample at several sample-to-detector distances (SDDs) for quantitative phase reconstruction.[24] Due to long SDDs, it utilizes phase contrast and requires the application of elaborate phase retrieval techniques prior to image reconstruction.[25,26] Its resolution depends on the source size and the magnification by choosing an appropriate SDD. TXM can either be used as a scanning or full-field technique. The scanning mode, which requires the focusing of the X-rays to a point and subsequent scanning of the sample, allows for simultaneous fluorescence (XRF) and/or diffraction (XRD) measurements. The focusing of the X-rays can be obtained by different optical systems, which are generally divided into refractive, reflective, and diffractive optics. Kirkpatrick–Baez mirrors, waveguides, compound refractive lenses, and Fresnel zone plates are the most notable among these.[27] Full-field imaging by contrast illuminates the whole sample at once and therefore results in much shorter imaging times.[28] Ptychography is a 2D scanning technique that obtains a diffraction pattern in each place from which quantitative phase projections can be retrieved. Through the combination with a rotation around the object's axis, tomographic imaging can be achieved at high spatial resolution.[29] Langer and Peyrin recently reviewed and compared the capabilities of NFHT, TXM, and ptychography for imaging of bone.[30] The image contrast and resolution of all three techniques are similar, reaching ≈50 nm, yet the acquisition time differs greatly.[27,31] Ptychotomography of specimens with a diameter of 40 μm is in the range of several hours,[29,32] while TXM and NFHT can be performed in minutes to hours,[28,33–35] depending on the required image quality. The advantage of ptychography and NFHT over TXM is the quantitative information on the phase the object that can be retrieved

from the images, yet the required algorithms for phase retrieval are significantly more computationally expensive.[30]

While direct imaging techniques yield insight on the sample morphology, its crystalline composition can be determined using XRD and spectroscopy techniques, such as XRF, can be used to yield better insight on the chemical composition. Moreover, small angle X-ray scattering (SAXS) can be used to investigate sample features in size ranges between those accessible by XRD and TXM. Scanning XRD, SAXS, and XRF can be performed in one experiment, by placing the SAXS detector in the X-ray path and the XRD and XRF detectors at an angle off the side of the sample stage. The spatial resolution of these complementary techniques depends on the size of the focal spot of the X-ray beam on the sample. Focal spots in the hundred nanometers to few micrometers in size are generated using aforementioned focusing optics. Absorbing slits that cut down the beam profile can also be used to achieve small micrometer-sized spots, but result in a stronger loss of brilliance than focusing optics.[27]

SAXS, XRD, and XRF are mostly performed in 2D but can be translated into 3D. Grain mapping, in particular, can be achieved by 3D XRD or diffraction contrast tomography (DCT) and allows for the orientation mapping of individual grains in a polycrystalline material.[36,37] Recently, SAXS has also been extended into 3D[38–40]; however, scanning times of the technique are in the range of days per sample, due to the scanning character of the technique and the requirement for a rotation around two axes. A general review detailing the use of the aforementioned techniques in materials science is that published by Maire and Withers.[22]

3. Alloy Development

The overall performance of an implant is strongly dependent on its microstructure and degradation properties. To obtain the desired property profile, the complete processing chain from raw material to the finished part needs to be controlled. This encompasses the material production (i.e., chemical composition, production route, and characterization of the primary microstructure), thermomechanical processing (heat treatments, mechanical processing, i.e., extrusion, rolling, etc.), and production of the part including forming and surface treatments.

3.1. Solidification

Traditionally alloys are manufactured by casting, i.e., melting and mixing the constituents and then solidifying the alloy in a mold. During solidification, the phases solidify according to the alloy composition and the cooling rate. Afterward, heat treatments may be used to achieve the dissolution of secondary phases into the α-Mg matrix. At this stage, or in exceptions directly after casting, the material can either directly be cut and processed into the desired implant shape, or it can be subjected to further thermomechanical processing, e.g., extrusion, rolling, or forging, to obtain the desired microstructure for the application. Traditional methods used to investigate the resulting microstructure morphology are light microscopy, scanning electron microscopy, and transmission electron microscopy. However, while these provide high-resolution insights, they are mostly limited to two dimensions making an analysis of the intermetallic phase distribution over large spatial scales impossible. By contrast, high-resolution SRμCT and SRnCT enable such analysis and are used depending on the size of the intermetallic particles. **Figure 1** schematically shows the use of different SR-based techniques for the determination of certain relevant parameters in Mg alloy development based on the required feature resolution.

3.1.1. α-Mg Dendrite Formation and Evolution

Mg dendrite growth and morphology during solidification are critical factors for the resulting mechanical properties. Thus, significant effort has been placed in obtaining a better understanding and control thereof. The initial use of SRμCT to this end was by using static imaging, yet with the onset of faster acquisition
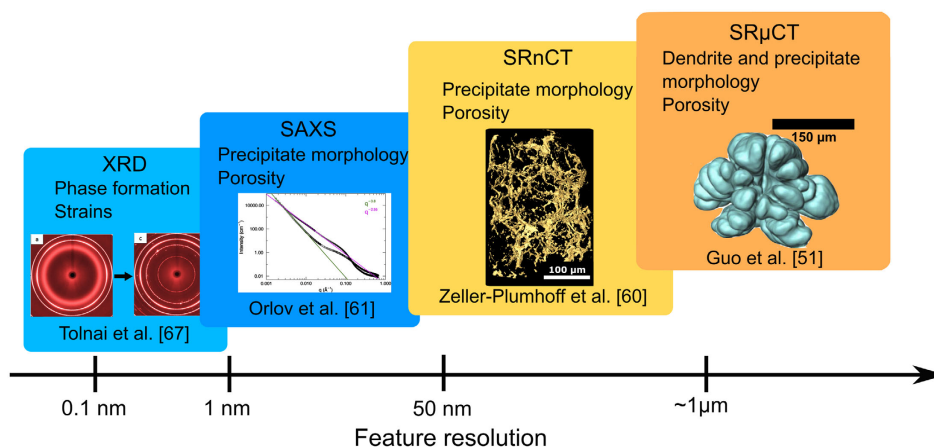
Figure 1. Schematic representation of different synchrotron radiation-based techniques to determine relevant parameters during Mg alloy development. SRμCT can be used to determine dendrite and precipitate morphology. Depending on the precipitate size, SRnCT or SAXS may be more suitable for their visualization. XRD is used to study the formation of phases during solidification. Figure from Guo et al. adapted under CC BY 4.0 License.[51] Copyright 2017 by the authors. Published by Elsevier. Figure from Zeller-Plumhoff et al. adapted under CC BY 4.0 License.[60] Copyright 2020 by the authors. Published by Springer Nature. Figure from Tolnai et al. adapted under CC BY 4.0 License.[67] Copyright 2018 by the authors. Published by MDPI. Figure from Orlov et al. reproduced with permission.[61] 2014, Elsevier.

ADVANCED
SCIENCE NEWS
www.advancedsciencenews.com

ADVANCED
ENGINEERING
MATERIALS
www.aem-journal.com

Figure 2. Composition of different experimental setup for in situ testing. a) Furnace for in situ tomographic imaging of solidification adapted under CC BY 4.0 License.[47] Copyright 2016 by the authors. Published by Elsevier. b) Dilatometer for in situ diffraction measurements during heating and solidification, reproduced under CC BY 4.0 License.[65] Copyright 2015 by the authors. Published by MDPI. c) Mechanical testing device for simultaneous diffraction measurements and radiography. Adapted with permission.[87] 2016, Elsevier. d) Loading rig 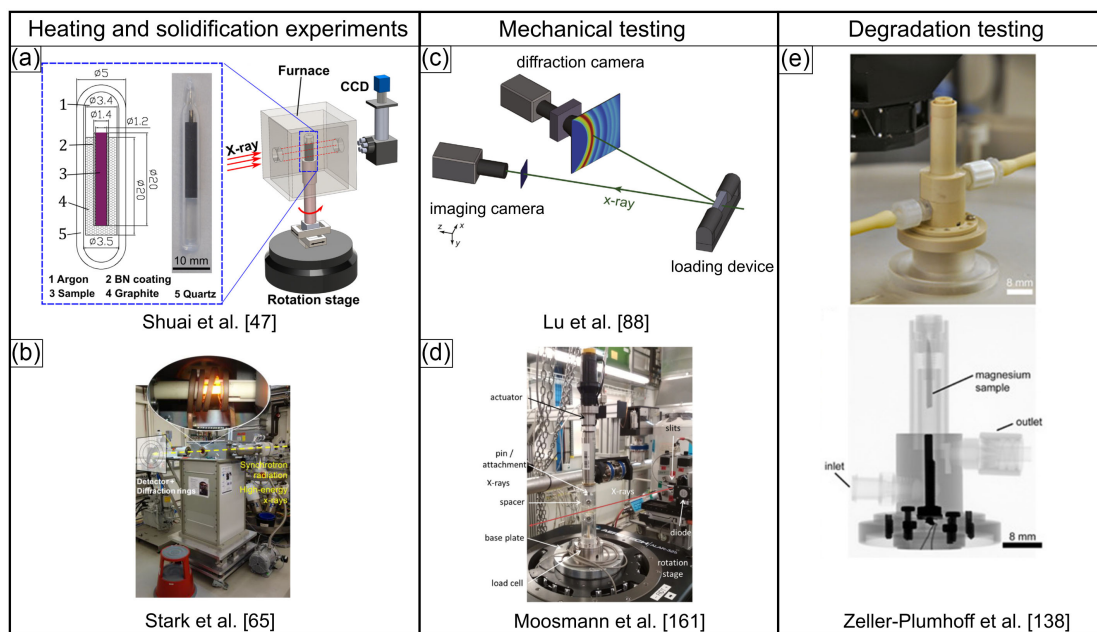for in situ tomography, adapted with permission.[159] 2019, SPIE. e) Flow cell for in situ tomography of Mg alloy degradation, adapted with permission.[137] 2018, Wiley.

times in situ imaging of dendrite growth is performed increasingly. Thus, in addition to the morphology of dendrites, their growth direction can be determined more precisely, as well as tip growth.[41] **Figure 2**a shows an exemplary experimental setup used for tomographic imaging of dendrite evolution. A range of Mg alloys with a high alloying content of heavy elements has been investigated and many have displayed similar dendrite morphologies comprising 18 branches. Specifically, a sixfold symmetry of α-Mg dendrites in the basal plane was observed for Mg–9Al,[42,43] Mg–40Zn,[44] Mg–30Sn, Mg–30Gd,[45] Mg–30Sn, Mg–25Al, Mg–10Ba, Mg–20Y,[46] and Mg–15Sn.[47] The primary dendrite growth direction in most cases was $\langle 11\bar{2}0 \rangle$,[48] while different authors identified either the $\langle 22\bar{4}5 \rangle$[44] or $\langle 11\bar{2}3 \rangle$[45,46] as second growth direction, with the difference being attributed to measurement uncertainty by some authors.[46]

However, in some cases dendrite growth appeared more complex. This was the case, in particular, for Zn-containing alloys, where an increase in Zn content was reported to lead to differences in branching morphology and a change in growth direction.[46,49,50] For higher Zn content, a preferred growth direction of $\langle 11\bar{2}1 \rangle$ instead of $\langle 11\bar{2}0 \rangle$ in the basal plane was reported. Interestingly, a Zn content of 38–40 wt%, in particular, led to a deviation in branching structure, revealing a hyperbranched morphology, while Zn contents below and above yielded the familiar sixfold symmetry.[49–51] Increasing contents of Al and Zn have also been reported to change the growth direction in the nonbasal plane from $\langle 11\bar{2}3 \rangle$ to $\langle 22\bar{4}5 \rangle$.[48]

Apart from alloying elements, the solidification method and cooling rate were found to have a significant influence on dendrite

morphology, but not growth orientation.[41,47,52] Specifically, Shuai et al. showed that slower cooling rates ($3\,^\circ\text{C}\,\text{min}^{-1}$) were found to result in globular dendrite morphologies, while faster cooling ($12\,^\circ\text{C}\,\text{min}^{-1}$) revealed sixfold symmetry for Mg–15Sn.[47] The authors found that the initial free growth phase is crucial in determining the ultimate dendrite morphology. The cooling rate also influenced the nucleation sites. For lower cooling rates, the nucleation was initialized preferably toward the sample border, while higher rates allowed for a homogeneously distributed nucleation. Guo et al. confirmed the influence of the cooling rates on the nucleation sites for Mg–25Zn–7Al, yet instead of affecting the branching morphology, the faster cooling rates specifically resulted in overall smaller grains.[41] Differences in Zn content have also been shown to result in differences in the influence of cooling rate.[51] Namely, a shift from 25 wt% Zn to 38 wt% led to a dependence of the coarsening rate on the initial cooling rate (3 vs $25\,^\circ\text{C}\,\text{min}^{-1}$).

The addition of nanoparticles, such as SiC, has been researched to enhance the alloy strength. Using in situ SRμCT Sillekens et al. showed that the presence of SiC nanoparticles in Mg–25Zn–7Al alloy led to a decrease in grain size and that certain nanoparticles may agglomerate during solidification.[53] Guo et al. confirmed the influence of SiC nanoparticles on dendrite size in Mg–25Zn–7Al and further showed that nanoparticles also led to a higher number of dendrites and a more even distribution of nucleation.[41] Moreover, the morphology of dendrites in the basal plane changed from the sixfold symmetry to a globular shape without preferred growth direction due to SiC nanoparticle presence. The authors attributed this to a local increase in Zn due to the obstruction of its diffusion by the

nanoparticles, leading to a similar effect as an overall Zn content of 38 wt%. T visualize SiC nanoparticles within the material, TXM can be used.[28]

Tolnai et al. used in situ SRμCT and XRD to study Mg–5Nd–xZn alloys ($x = 3$, 5, 7 wt%).[54] XRD yielded insight into the temperatures at which α-Mg and certain intermetallic phases formed, while tomographic imaging revealed the coarsening dendrite shape during cooling and the developing pore network. The addition of Zn was found to stabilize the $Mg_3(Nd,Zn)$ phase in particular and the $Mg_{50}Zn_{42}Nd_8$ phase formed for Mg–5Nd–5Zn.

3.1.2. Morphology of Secondary Phases

In addition to studying the Mg dendrite morphology, SRμCT has been used to study the evolution of secondary phase morphology of a range of alloys, the first time so in 2007 by Witte et al. who investigated AZ91D in as-cast and extruded condition.[55] The net-like β-phase morphology was shown to break up during extrusion and Al–Mn particles agglomerated and aligned along the extrusion direction. If the size of precipitates is small, SRnCT may be more appropriate for their investigation. NFHT has been used to assess the microstructure of a range of alloys, including AlMg7Si4, Ti alloys, and dual-phase steel.[56–59] It was shown, in particular, that changes in the Mg_2Si phase morphology due to heat treatment can be observed in AlMg7.3Si3.5 using NFHT.[56] Recently, NFHT was also used to visualize and quantify the changes in intermetallic particle structure due to severe plastic deformation in ZK60 alloy (Mg–5.78Zn–0.44Zr).[60] The intermetallic particle structure displayed a more plate-like, continuous morphology after extrusion and broke up into smaller particles due to the deformation. While NFHT can generally be used to assess intermetallic particles in 3D, it results in strong image artifacts due to phase wrapping, if the photon energy is too low given the sample size and density.[60] This is a general shortcoming of NFHT for the use in materials science as the selected photon energy is generally constrained by the available X-ray optics. Few light sources, among it the European Synchrotron Radiation Facility (ESRF), enable holotomographic imaging at energies significantly greater than 13 keV.[58] In the same study of the ZK60 alloy, TXM with Zernike phase contrast was used to circumvent the image artifacts from NFHT. Small differences in intermetallic particle distributions were observed between both techniques, which were likely to stem from differences in magnification.[60] In addition, SAXS can be used to analyze the morphology of intermetallic particles indirectly, if the resolution of SRnCT methods is insufficient. The ZK60 alloy imaged using NFHT, for example, had previously been analyzed using SAXS, where the same change in particle morphology due to severe plastic deformation was observed.[61]

No further use of TXM for the study of Mg alloys has been reported in the literature so far. This may partly be due to the cumbersome sample preparation procedure required for TXM. To prepare samples of the required size, the metal needs to be processed down 25 μm in diameter, depending on the field of view. This can either be achieved by cutting, grinding, and polishing samples, which is destructive to the overall sample. Instead, focused-ion beam milling can be used to mill a sample

from a region of interest with damage only to the parts of the sample immediately adjacent.[62] However, depending on the desired sample size and machine used, this process can take up to 1 day per sample. TXM has been used for the analysis of other alloying systems, however, including an in situ analysis of the compressive behavior of Al–Cu alloys. Specifically, Kaira et al. demonstrated the influence of intermetallic phase distribution and morphology on the deformation behavior.[63] We therefore expect that TXM will be used more frequently for the analysis of Mg alloys in the future.

3.1.3. Composition of Secondary Phases

Synchrotron diffraction is the SR-based technique most often applied to analyze Mg alloy microstructural changes, in particular to study the phase transformation during heating and cooling and to develop phase diagrams. The detection limit of the technique lies at around 1 vol%, while the crystal lattices have to fulfill the Bragg equation to be detected.

The study of phase dissolution and formation can be performed in situ using a dilatometer setup[64,65] at high-energy beamlines, which enables heating of the sample via an induction coil and is equipped with entrance and exit windows for the transmission of the X-ray beam (see, e.g., Figure 2b). Thus, the phase transformations in Mg–4Y–3Nd (WE43) alloys during cooling could be correlated with thermodynamic calculations while additionally displaying the presence of certain phases ($Mg_{14}Y_4Nd$) that had not been predicted theoretically.[66] **Figure 3** shows an exemplary image of WE43 powder XRD signals during heating and solidification in a dilatometer. Moreover, the phase evolution dependent on increasing addition of certain alloying elements to binary alloys can be studied, such as Zn
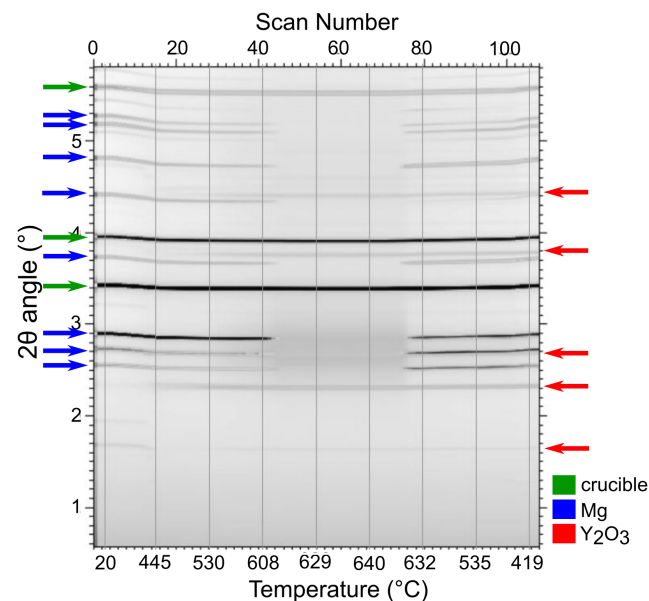
Figure 3. X-ray diffraction signal of WE43 powder during heating and solidification (left to right) at a photon energy of 103.4 keV. The image shows the disappearance and appearance of different phases as they go into solution and solidify. A number of relevant phases have been identified, as indicated by colored arrows.

ADVANCED
SCIENCE NEWS

www.advancedsciencenews.com

ADVANCED
ENGINEERING
MATERIALS

www.aem-journal.com

(3, 5, and 8 wt%) to Mg–4Nd.[67] Tolnai et al. found that $Mg_5Nd_8Zn_{42}$ phases were present for 5 and 8 wt% Zn and $Mg_3(Nd,Zn)$ for all alloys with Zn addition. The experimentally observed phases differed somewhat from those predicted using thermodynamic calculations, thus the data could be used to improve the underlying databases.

In the same manner, the dissolution of oxides in Mg can be determined, such as CaO in Mg to form Mg_2Ca and MgO.[68] This is of particular interest, as Ca addition enhances biocompatibility and creep resistance in some cases.[7] Medina et al. studied the influence of Ca, Mn, and Ce mischmetal (CeMM) additions to Mg–6Zn–1Y alloy following casting during heating to 650 °C, and following extrusion with particular respect to the quasicrystalline I-phase whose presence results in favorable properties for the application of an Mg alloy as a structural material.[69] Mn additions did not affect the presence of the I-phase, while alloys after Ca and CeMM addition displayed no I-phase. Moreover, CeMM led to a formation of the T-phase and W-phase, with the latter also being present after Ca addition.

However, in some cases XRD may be insensitive to certain phases, depending on their volume fraction, thus a correlation with other methods is often performed.[70] In addition to phase formation during solidification, XRD can be used to study phase formation due to certain processing steps and techniques, such as aging of the material[70] or explosive welding.[71] By assessing the lattice spacing shift, peak broadening, and changes in intensities, internal stresses and dislocations in the material due to processing, such as equal channel angular pressing (ECAP),[72] laser beam welding,[73] or friction stir welding,[74] can be determined. The stresses can be spatially resolved by adjusting the beam size and position.

Of course, studying the evolution of phases using in situ XRD is not limited to alloys manufactured via the wrought route, but can be applied similarly to study the behavior of powders for powder metallurgy (PM).

3.2. Powder Metallurgy

In addition to the traditional casting route, Mg alloys can also be processed by sintering, using binder-based PM routes as there are metal injection molding (MIM) and additive manufacturing (AM), as well as melting-based AM such as selective laser melting (SLM). Moreover, powder extrusion can be used to raise the materials maximum potential and properties but is only appropriate to perform semifinished parts. Mg powder particles display a light oxide layer.[75] Due to insolubility of oxygen in Mg as well as its high oxygen affinity, sintering and melting techniques of Mg alloys require an atmosphere free from oxygen by application of inert gas, such as Ar, at high temperatures.[76] The sintering process generally results in a nearly dense microstructure, providing some residual porosity depending on the alloying system, sintering temperature and time, and applied pressure.[76,77]

As the porosity determines the mechanical and degradation properties of the material, it is of particular interest. Depending on the pore size, SRµCT can be used to determine the porosity,[78] as well as indirect techniques such as SAXS.[79] The critical pore size that can be resolved depends

on the technique's feature resolution (see Figure 1, i.e., with SRµCT pores measuring few micrometers can be resolved). **Figure 4**a,b shows two examples where µCT was used to determine the sample porosity for samples produced by SLM and sintering. While SRnCT similarly enables the investigation of the porosity, its use has not yet been reported. SRnCT is also particularly useful to understand the processes occurring during sintering itself. The authors have recently used TXM to visualize (partly) sintered powder particles as a proof-of-concept, and are able to identify the neck formation between two particles (Figure 4c) as well the partial breaking up of a sputtered MgO layer by liquefied Mg–10Ca (Figure 4d). A broken-up oxide layer is visible also between the two sintering particles in Figure 4c. Extending SRnCT methods for in situ measurements of the sintering process will allow for the observation of the destabilization of the oxide layer in a dynamic manner, as well as the formation
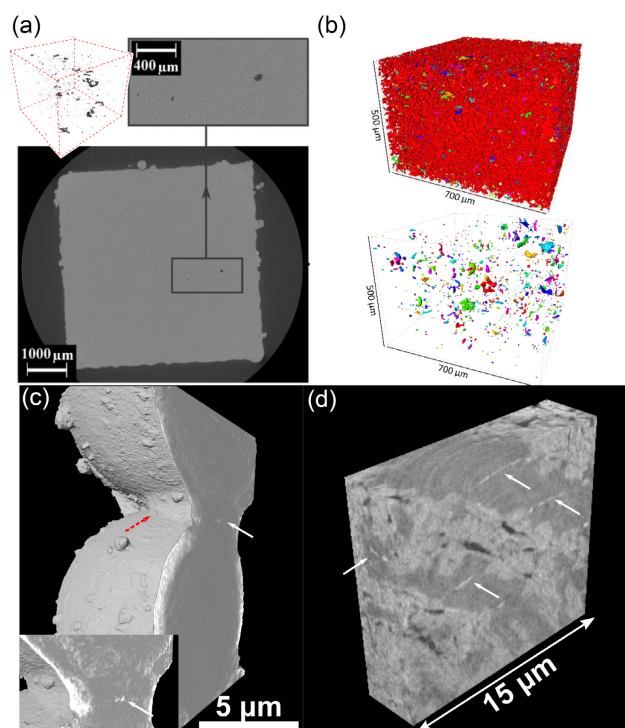
Figure 4. a) µCT slice of a porous Al–Si10–Mg specimen produced by selective laser melting with inset of the 3D volume rendering of all pores. Adapted with permission.[187] 2016, Elsevier. b) 3D volume renderings of the pores in two Mg–0.6Ca samples produced by sintering at different temperatures, with 21% (top) and 3% (bottom) porosity. The components' color describes their connectivity. Adapted under CC BY 4.0 License.[77] Copyright 2020 by the authors. Published by Elsevier. c) Slice through TXM tomographic image volume showing two Mg–0.9Ca sinter particles and the connecting neck (red arrow). The inset displays a zoom into the neck region between the two powder particles, in which remnants of the oxide layer are visible (white arrows). d) 3D rendering of a sputtered multilayer sample containing Mg–10Ca and a 200 nm-thick MgO layer. The sample was heated to 540 °C for 2 h. MgO is visible in white, and pores in dark. Different phases are visible, with the darker grey likely to be the original Mg–10Ca. It appears that the MgO layer (white arrows) was partly broken up as it's no longer visible in the lighter grey phase. The sample width and height are ≈15 µm.

**ADVANCED
SCIENCE NEWS**

www.advancedsciencenews.com

**ADVANCED
ENGINEERING
MATERIALS**

www.aem-journal.com

of secondary phases. This will enable a more comprehensive understanding of the sintering process, for a better control thereof, in particular, for the development of new alloying systems.

3.3. Thermomechanical Processing

The material response to thermomechanical loads in case of various Mg alloys has been the subject of numerous SR-based investigations. These experiments show the main operating deformation mechanisms at different temperatures and deformation rates, how the load is distributed among the phases,[80] and how the texture changes.[81] However, while these experimental conditions are only partially relevant during the service life of an implant, the results of these investigations are essential to optimize the processing routes and to gain control over the resulting microstructure. A lot of focus in thermomechanical testing of Mg alloys has been placed on studying AZ31 (Mg–3Al–1Zn) and other Al-containing alloys because AZ31 is a benchmark for structural applications. The use of Mg alloys containing Al as implant material is, however, discouraged, as Al enrichment in the brain is associated with Alzheimer's disease.[82] Instead, Ca-, Zn-, or rare earth (RE)-containing Mg alloys are of higher interest for implant materials. Figure 2c,d shows examples of in situ testing rigs for mechanical tests at diffraction or tomographic imaging instruments.

3.3.1. Mg–Al Alloys

With respect to extruded AZ31 it was shown, in particular, that $\{10\bar{1}2\}\langle10\bar{1}1\rangle$ twinning is dominating during uniaxial cyclic deformation along the extrusion direction.[83] The initial texture was found to influence the mechanical behavior as different deformation systems are activated.[84] Different strains are required to activate twinning for tensile and compressive loading.[85] During tensile testing, $<a>$ basal slip and $\{10\bar{1}2\}$ tensile twinning are activated, while pyramidal $<c+a>$ slip is additionally activated during compression.[86] Anisotropic deformation of extruded AZ31 suggested that $\{10\bar{1}2\}$ twinning was responsible for the higher strain hardening rate for applied loads parallel to the extrusion axis.[87] Similarly, a relationship between loading and rolling direction was suggested for rolled AZ31B.[88] In normal direction, $\{10\bar{1}2\}$ tensile twinning and detwinning were increasingly observed. In rolling direction and its transverse extension, twinning/detwinning and nonbasal $<a>$ dislocation slip were high, while in normal direction the c-axis of most grains was aligned with the loading direction, leading to low ductility. Detwinning of $\{10\bar{1}2\}$ tensile twins during unloading of rolled AZ31, on the contrary, was independent of the loading direction and previous twin activation.[89]

Temperature influences the deformation mechanisms, with basal slip being dominantly observed during compression testing at temperatures between 150 and 300 °C, while twinning was not visible.[90] A reinforcement of AZ31 with 10 vol% SiC nanoparticles revealed no changes in dislocation types during deformation. Specifically, basal slip and $\{10\bar{1}2\}\langle10\bar{1}1\rangle$ dominated in tensile and compression testing, respectively. However, SiC

particle addition led to a reduction in twin growth and nucleation, and accumulated strains during compression.[91–93] The onset of faster detector technologies enabled the study of high strain rates such as $2500\,s^{-1}$ on twinning during compressive loading in situ, which revealed the importance of alloying elements in AZ31B to reduce the speed of $\{10\bar{1}2\}\langle10\bar{1}1\rangle$ twin growth.[94] In many cases, in situ XRD measurements are combined with elastic plastic self-consistency (EPSC) modeling to better understand dislocation modes.[90,95,96]

3D XRD and differential-aperture X-ray microscopy (DAXM) enable investigating twinning behavior in a spatially resolved manner at high resolutions of up to 0.7 μm.[97–100] Thus, Aydiner et al. were able to study the stress state of a tensile twin formed during compression with respect to its parent grain, which they found to be generally lower along the compression axis, but higher along the c-axis of the parent.[97] Lynch et al. developed a Laue-based technique for in situ micro-XRD to simultaneously measure slip and twinning events at high spatial resolution.[99] Thus, they showed that basal slip occurred first, followed by twinning and the evolution of accommodation slip in extruded AZ31 during stepwise tensile testing (loading direction perpendicular to extrusion direction) up to 60 MPa. Again, twinning of type $\{10\bar{1}2\}\langle10\bar{1}1\rangle$ was observed. This technique was subsequently used to study the behavior of AZ31 at higher loads between 64 and 73 MPa.[101] 3D XRD and more specifically grain mapping also enable a correlation between material microstructure and crack growth measured using SRμCT during tensile testing.[102] King et al. showed that cracks propagate through grains in Elektron21, with a tendency for growth orientation along the basal plane. The crack opening modes were later on computed via digital volume correlation (DVC) as mixed mode opening that was particularly influenced by boundaries disrupting the basal plane growth.[103] In addition to XRD measurements, SRμCT was performed after tensile testing to study the crack morphology in AZ31 with addition of 0.2–0.3 wt% Mn. Depending on the material thickness, void nucleation and growth could be observed,[104] while the crack mechanism in thin sheets could be identified as void-sheeting of nanovoids.[105]

3.3.2. Mg–Y Alloys

Mg–Y alloys show a high creep and corrosion resistance, especially when combined with RE elements.[7] Alloy WE43, in particular, has found application as an implant material and in the composition developed by Syntellix AG (Hanover, Germany) it is the only Mg-based fixation screw with a CE mark. Similarly, Biotronik AG (Bülach, Switzerland) has developed a proprietary WE43-based alloy that is used in Biotronik's (Berlin, Germany) Magmaris stent, the only Mg-based stent with a CE mark. Nevertheless, research in Mg–Y alloys is ongoing, with some researchers investigating WE54[106,107] and a large part of research focusing on long-period stacking order (LPSO) structures, which display high yield strengths both at room and elevated temperatures.[108] Their specific tensile yield strength, in particular, was found to be higher than conventional Ti–6Al–4 V alloy. SR-based SAXS and XRD measurements have been used to understand LPSO structures mostly in Mg–Y–Zn alloys. Certain LPSO structures are more stable during heating

(18 R vs 10 H), as shown for $Mg_{85}Y_9Zn_6$[109] even at as low cooling rates as 20 K min^{-1} tested with $Mg_{88}Y_8Zn_4$[110]; however, the addition of RE elements, i.e., Nd, gives rise to the 14 H structure as shown for $Mg_{97}Y_2Zn_1$.[111] In situ measurements revealed the formation of LPSO structures during heating that arise from amorphous material in the form of clusters that crystallize and build the microstructure with distinct distances between cluster and introduced stacking faults due to a local lattice distortion.[112–114] A comparison of $Mg_{85}Y_9Zn_6$ and $Mg_{85}Gd_9Zn_6$ showed that temperature was the deciding factor for the transition from hexagonal close packed to LPSO.[115] In situ mechanical testing of Mg–Y alloys containing LPSO phases has been performed to investigate the active deformation mechanisms and load transfer to the LPSO structure at different temperatures.[116–120]

3.3.3. Mg–Zn Alloys

The addition of Zn increases alloy strength[7] and ZK alloys (Mg–xZn–yZr), in particular, have been shown to display good corrosion and mechanical properties.[61,121,122] Buzolin et al. studied ZK40 alloy with additions of 2 wt% of Gd, Nd,[123] or CaO or Y[124] during compression testing using in situ XRD. The compressive yield strength was increased for both Gd and Nd additions, which was attributed to the presence of intermetallic particles, and dynamic recrystallization was observed in ZK40 (continuous) and ZK40–2Gd (discontinuous), with twinning being observed only for ZK40–RE at 350 °C. Y addition showed a greater effect than CaO in increasing 0.2% proof strength during compression, which coincided with work hardening in the material. The intermetallic phases formed along grains after addition of CaO seemed to contribute little strength, leading to a similar loading behavior of ZK40 and ZK40–2CaO. Both ZK40 and ZK40–2Y showed dynamic recrystallization during loading, which was not visible for CaO addition. The addition of Nd to hot-rolled Mg–1Zn, on the contrary, resulted in the weakening of the alloy texture and lower tensile yield following Nd addition, due to an increased activation of basal slip.[125]

3.3.4. Mg–RE Alloys

Mg–RE alloys are of high interest for the use as implant material, due to the control of the corrosion rates through the addition of RE elements.[5] The effect of Zn addition to Mg–xNd ($x = 3, 4, 5$ wt%) was studied extensively by Tolnai and Gavras et al. both at room and elevated temperature and as a function solution treatment.[126–128] Solution treatment and temperature strongly influenced the observed behavior, though generally no or only very low (<3 wt%) addition of Zn led to the highest reinforcement from intermetallic particles and most stable microstructure.

Other researchers studied the addition of Ce[129,130]; however, Ce is not investigated in great detail for clinical applications, as it has been shown to reduce cell viability significantly[4] and Mg–Ce alloys degrade faster than other Mg–RE alloys in vivo.[131]

3.3.5. Mg–Li Alloys

The influence of deformation on the structure of Mg–5Li has been studied, which is an alternative alloying system for lightweight structural applications,[132] but is similarly of interest for biodegradable implants.[133] Lentz et al. studied Mg–4Li and Mg–4Li–1Al using in situ XRD and SCEP modeling to find that $\{10\overline{1}2\}\langle 10\overline{1}1\rangle$ twinning seems to be reduced in these alloys, which led to an asymmetry in yield strength for tensile and compression testing.[134] Moreover $<c + a>$ pyramidal slip activity was increased. Al addition further increased yield strength.

4. Implant Characterization In Vitro and Ex Vivo

4.1. In Vitro Degradation Analysis

Once the material has been developed based on the desired specifications in terms of its microstructure, immersion tests in aqueous media are conducted under physiological conditions to test its degradation properties. The immersion media are selected to mimic body fluids, but vary in terms of ionic components and complexity, as they can be enriched with organic components, such as amino acids and proteins.[10] In addition to the degradation of the metal, the degradation process can include the formation of a degradation layer due to the precipitation of salts forming from the ionic components in the medium. Depending on the composition of the medium and the environment, these are mainly Mg- or Ca-based phosphates, carbonates, and hydroxides. The degradation process of Mg is a highly dynamic process, which depends on the environmental conditions (temperature, gaseous environment, pH), the medium composition, hydrodynamic conditions, and, naturally, the alloy itself.[10] Of course, different media and environments may be selected if testing the corrosion resistance of Mg alloys for other applications, e.g., as lightweight structural metals.

SRμCT above and below the Y K-edge of 17 keV was used by Davenport et al. to study the role of Y on WE43 alloy corrosion in 0.1 M NaCl at a pH of 10.[135] Due to the energy variation, the difference image of the sample displays the element distribution in 3D. In situ corrosion experiments were performed by using a simple liquid-filled container in which the sample was immersed during imaging. It was shown that as-cast samples degraded more heavily than T6 heat-treated samples, which displayed a more homogeneous microstructure. However, a direct spatial correlation between precipitates and corrosion was not provided and the corrosion was evaluated only qualitatively.

By designing a bioreactor coupled flow cell (Figure 2e), SRμCT has been successfully used to image the degradation of prospective implant materials Mg–2Ag and Mg–10Gd–1Nd in α-Modified Eagle's Medium (α-MEM) in situ.[136,137] Thus, a quantitative analysis of the degradation process and its homogeneity in 3D over time was performed. Specifically, the degradation rate (DR) [mm year^{-1}] was calculated as

$$DR = \frac{V_0 - V_t}{A_0 t} \tag{2}$$

with V_0 and A_0 being the initial implant volume and surface, respectively. V_t is the residual metal volume following degradation over time t (scaled to years). Consequently, the nonlinear nature of the degradation process that is normally observed by fitting discrete data points[138] was verified in a more continuous manner.[137] Moreover, due to the coupling to a bioreactor and

allowing for continuous flow, the long-term experiment could be performed at stable physiological conditions and without an exceeding alkalization of the sample environment. The experimental setup is also flexible with respect to the fluid used for the degradation test; simple ionic solutions can be used, as well as more complex cell culture media and even the addition of proteins is possible, as the mixing in the bioreactor and the flow prevent clogging of the tubing systems.

When performing such in situ experiments, it is pivotal to tailor the design of the experimental cell to the experiment type and optimize it both for the conditions that should be achieved, e.g., fluid flow, and the required image quality, in terms of contrast and noise. For example, the diameter of the cell needs to be adjusted depending on the available photon energies to ensure sufficient transmission through the liquid and the sample. Furthermore, in imaging experiments, the rotation of the cell must be enabled for at least 180° with as little obstruction of the field of view as possible.

In many cases of controlled Mg alloy degradation, a stable degradation layer consisting of precipitating salts forms on the degrading sample surface[139] This layer acts as a protective film and its composition depends, for example, on the ions present in the immersion medium and the alloy, as well as all other environmental conditions stated earlier. In situ XRD experiments can be performed to study the time-dependent process of crystallization of certain precipitates that form during degradation. In an experiment unrelated to Mg implants, it was, for example, shown that pH strongly influenced the lattice structure in which previously amorphous calcium carbonate crystallized.[140] These experiments, if replicable under physiological conditions, can lead to a better understanding of the precipitation processes occurring on the implant surface during degradation. Apart from XRD, synchrotron Fourier transform infrared (FTIR) microspectroscopy can be used to study the composition of the degradation layer composition, which enables also the identification of amorphous compounds.[141] Thus, Agha et al. were able to show that Ag addition leads to a preferred formation of $MgCO_3$, while Ca and P formed compounds that were similar to hydroxyapatite, the crystal component of bone, in the presence of osteoblasts. The protective layer contains a pore network that facilitates and controls ion transport during degradation. The pore network morphology can be determined using TXM, as recently shown.[142]

In addition to studying the material behavior during degradation, its interaction with cells needs to be determined, to study the influence of Mg and alloying elements on cell survival and function. This is of particular importance in cases where alloying elements are disputed for their toxicity, such as Gd.[143,144] To this end, SRnCT and XRF can be used, which can reveal the intracellular distribution even of light elements Mg, C, N, O, and Na in whole cells.[145,146] Outside the context of Mg implants, it was thus shown, for example, that a colocalization of Zn and Ca and P can be observed during the mineralization process of mesenchymal stem cells, which strengthens the understanding of the role of Zn as nucleation site.[147] Moreover, a combination of SRnCT and X-ray absorption near edge structure (XANES) showed that after 10 days of cell differentiation Ca depositions are mostly present in the form of crystalline hydroxyapatite. Clearly, the same techniques could be applied to study the effect

of degrading Mg implants and alloying elements on the mineralization process in cell culture experiments in a more localized manner. In the future, such experiments may be envisaged to be performed in situ, as the coupling to a bioreactor could maintain cell culture conditions in a fluid cell. However, as mentioned earlier, the feasibility of the experiment may depend on the thickness of the fluid layer and the required photon beam energy, to ensure sufficient detectability of transmitted/emitted X-rays.

4.2. Ex Vivo Characterization

Following successful in vitro testing and cytocompatibility tests, implant materials are tested in animal experiments. Different animal models can be used; small animal models using mice or rats are initially used due to their relative ease and lower costs, while large animal models include sheep whose bone morphology is closer to that of humans. Rabbit models can be used as an intermediate step. Magnesium implants are often implanted into the tibia or femur of the animal, specifically into the diaphysis of the long bone.[148,149] However, depending on the scientific question different implantation sites are used, such as the epiphysis, metaphysis, or intercondylar notch.[133] Healing times are selected based on the scientific question and bone healing stage under investigation. During healing in vivo imaging techniques such as CT, magnetic resonance imaging, or positron emission tomography are used to investigate bone healing and implant degradation over time. Subsequently, animals are sacrificed and bone explants surrounding the implant are prepared for further analysis. As bone is a hierarchical material,[150] different structural levels need to be investigated for the influence of Mg implants thereon. **Figure 5** shows the different hierarchical levels of bone for better understanding. **Figure 6** shows the different synchrotron- and laboratory-based techniques that can be used to this end and the information that they reveal. Naturally, they can be used in a sequential manner, such that all hierarchical levels are assessed.

SRμCT is used for the analysis of the osseointegration, i.e., the contact of the degrading implant with the newly formed bone and the implant degradation in general. The degradation rate can be determined in the same manner as during in vitro testing, and additionally bone-to-implant contact (BIC) and bone-volume over total-volume (BV/TV) are standard parameters that are calculated to assess osseointegration. For SRμCT measurements, the explants can be embedded, critically point dried or imaged fresh-frozen, depending on further analyses. To date, only a small number of SRμCT experiments have been conducted, as shown in **Table 1**.

Witte et al. first used SRμCT to study AZ91D and LAE442 alloys implanted into the intramedullary cavity of guinea pig femora with a healing time of 18 weeks.[151] AZ91D was almost completely degraded after 18 weeks, while LAE442 was mostly intact with localized pitting corrosion in some areas. However, the reported degradation rates were lower than the presented volume measurements suggested. Therefore, the degradation rates shown in Table 1 have been updated according to the presented volume loss numbers in the article. It was subsequently shown by the same group using SRμCT that a MgF$_2$-coating further increased the corrosion resistance of LAE442 alloy implants in
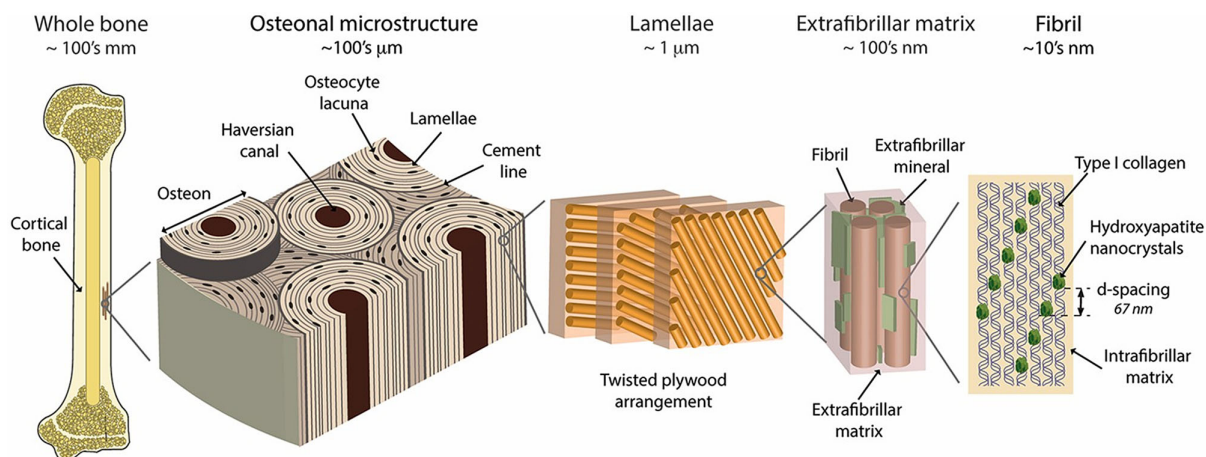
Figure 5. Hierarchical structure of bone, reproduced under CC BY 4.0 License.[188] Copyright 2016 by the authors, published by Springer Nature. Different SR techniques can be used to assess the different hierarchical levels. SRµCT reveals the microstructural level, which enables the calculations of parameters such as BIC, while SRnCT reveals the structures of the LCN and bone lamellae. To visualize the bone ultrastructure, i.e., the collagen fibers and HAP, SAXS, and XRD can be used, respectively.
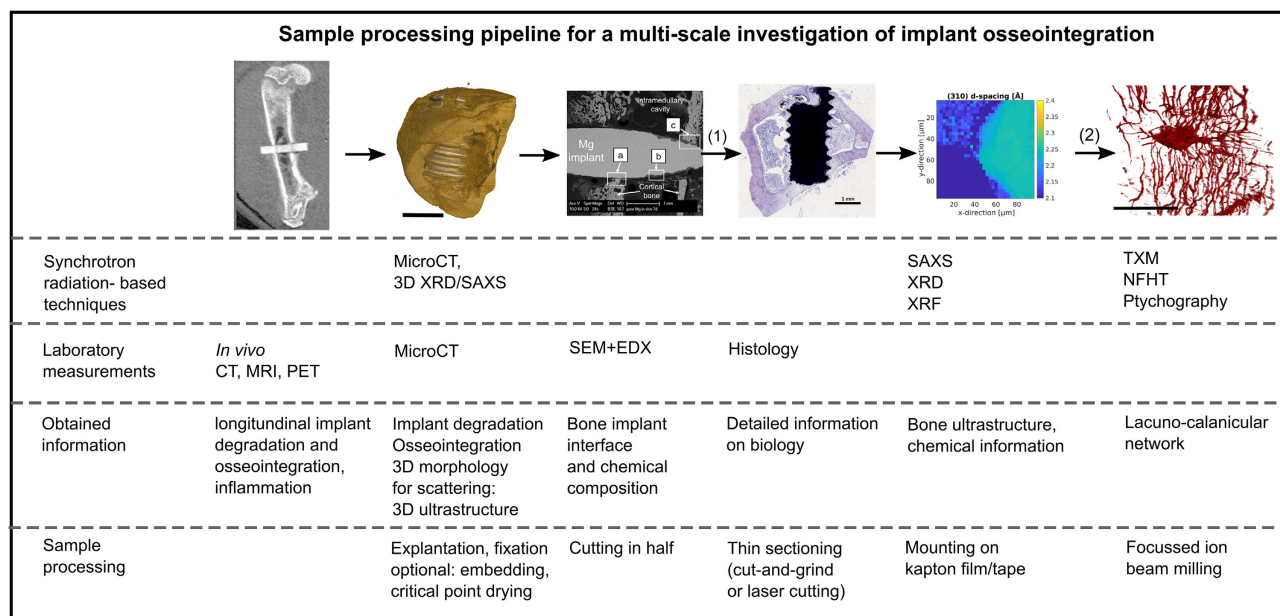

Sample processing pipeline for a multi-scale investigation of implant osseointegration

Synchrotron radiation-based techniques		MicroCT, 3D XRD/SAXS		SAXS XRD XRF	TXM NFHT Ptychography
Laboratory measurements	*In vivo* CT, MRI, PET	MicroCT	SEM+EDX	Histology	
Obtained information	longitudinal implant degradation and osseointegration, inflammation	Implant degradation Osseointegration 3D morphology for scattering: 3D ultrastructure	Bone implant interface and chemical composition	Detailed information on biology	Bone ultrastructure, chemical information	Lacuno-calanicular network
Sample processing		Explantation, fixation optional: embedding, critical point drying	Cutting in half	Thin sectioning (cut-and-grind or laser cutting)	Mounting on kapton film/tape	Focussed ion beam milling

Figure 6. Sample processing pipeline for the multiscale investigation of implant osseointegration covering all hierarchical levels of bone. Some levels can be assessed using synchrotron radiation-based techniques, while other levels require complementary laboratory-based techniques. The attainable information is listed as well as required sample processing steps. (1) and (2) indicate two different branches along the pipeline; following cutting the sample into halves after µCT imaging, e.g., for SEM+EDX measurements, (1) thin sections can be produced for histology and scattering experiments, or (2) small samples can be prepared for nanotomographic imaging. The in vivo image was adapted under CC BY 4.0 license,[9] copyright 2016 by the authors, published by Elsevier. No scale bar was given, but the Mg pin is 10 mm long. The histology and XRD images were adapted under CC BY 4.0 license.[149] Copyright 2020 by the authors, published by Elsevier. The SEM image was adapted under CC BY-SA license.[189] Copyright 2017 by the authors, published by the AO Research Institute Davos. The scale bar in the 3D bone rendering is 2 mm, that of the histology is 1 mm, and that of the lacuna rendering is 10 µm.

the femoral condyle of rabbits.[133] However, pitting corrosion was still reported for both implant types. Guan et al. studied a brushite-coated Mg–3.1Nd–0.2Zn–0.4Zr alloy in rabbit mandible defects with a healing time of 1, 4, and 7 months and calculated degradation rates based on SRµCT images.[152] The degradation rate first decreased between month 1 and 4 and then increased

until month 7, at which point the mechanical integrity of the screw neck was compromised. Galli et al. used SRµCT to evaluate the degradation of Mg–2Ag, Mg–10Gd, and WE43 in rat tibia at 1 and 3 months postimplantation and were the first to report a quantification of the BIC based on the images. Screws were implanted perpendicular to the long axis of the bone. **Figure 7**

Table 1. Summary of performed SRμCT studies of Mg alloy implant osseointegration for which the degradation rate was quantified.

Alloy	Implant shape	Animal	Implantation site	Sample fixation	Healing time [weeks]	Degradation rate [mm year^{-1}]	Bone-to-implant contact [%]	Ref.
AZ31D	Pin	Guinea pig	Femur intramedullary cavity	Fixed[a)]	18	0.90[b)]	n.a.	[151]
LAE442	Pin	Guinea pig	Femur intramedullary cavity	Fixed[a)]	18	0.36[b)]	n.a.	[151]
LAE442	Pin	Rabbit	Femoral condyle	Fixed[a)]	2	0.58 ± 0.06	n.a.	[133]
					4	0.46 ± 0.11		
					5	0.43 ± 0.10		
					12	0.31 ± 0.06		
LAE442 + MgF$_2$	Pin	Rabbit	Femoral condyle	Fixed[a)]	2	0.40 ± 0.03	n.a.	[133]
					4	0.29 ± 0.00		
					5	0.14 ± 0.02		
					12	0.13 ± 0.03		
Mg–3.1Nd–0.2Zn–0.4Zr + brushite coating	Screw	Rabbit	Mandible	n.a.	4	0.161 ± 0.075	n.a.	[152]
					12	0.097 ± 0.013		
					28	0.218 ± 0.03		
Mg–2Ag	Screw	Rat	Tibia diaphysis	Fixed[c)], critical point dried	4	1.01 ± 0.11	10.2	[148,153]
					12	0.49 ± 0.07	4.7	
Mg–10Gd	Screw	Rat	Tibia diaphysis	Fixed[c)], critical point dried	4	1.15 ± 0.19	27.4	[148,153]
					12	0.39 ± 0.04	48.4	
WE43	Screw	Rat	Tibia diaphysis	Fixed[c)], critical point dried	4	0.82 ± 0.10	17.7	[148,153]
					12	0.37 ± 0.03	45.2	

[a)]Fixed in 10% paraformaldehyde; [b)]Corrected values calculated based on volume loss measurements given in publication; [c)]Fixed in isopropanal.
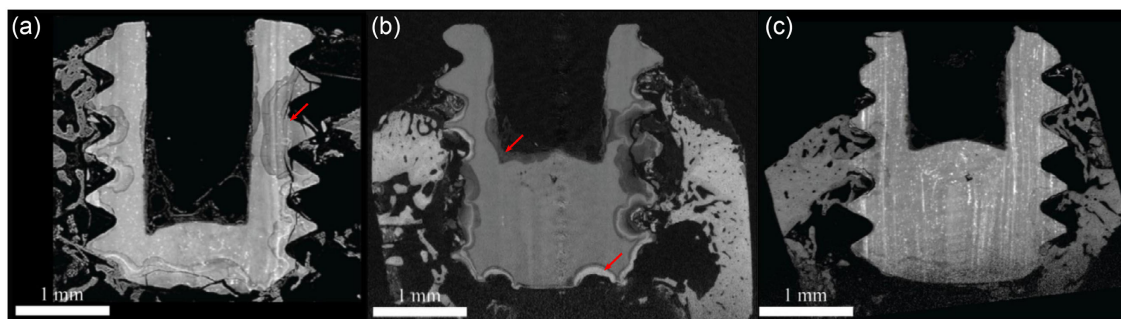

Figure 7. Slices of the tomographic reconstruction of bone explants containing a) Mg–2Ag, b) Mg–10Gd, and c) WE43 screw implants after 1 month of healing obtained using SRμCT. Both the bone and the screws are well visible. The screws contain different variation of grayscales pertaining to the degradation layer (red arrows) and secondary phases (bright particles or strings), adapted with permission.[148] 2017, SPIE.

shows slices of the tomographic reconstruction of one sample per alloy after 1 month of healing.

Mg–10Gd was shown to display a higher initial degradation rate than the other alloys, but a decrease in the degradation rate was observed between the first and third month. WE43 degraded the slowest for both time points, while Mg–2Ag showed a similarly high initial degradation as Mg–10Gd and less dampening thereof over time.[148] There was no direct correlation between degradation rate and BIC, as BIC for Mg–2Ag was smaller than for Mg–10Gd and WE43 and varied strongly for Mg–10Gd after 3 months. Notably, Galli reported a significantly higher BIC for Ti than for Mg implants (80% for Ti vs <50% for Mg

alloys).[148,153] In addition to the selected alloy, the degradation rate of Mg alloys is strongly influenced by the implantation site, i.e., parts of implants in contact with bone behave differently to those in contact with soft tissue.[154] In the study by Willbold et al. AZ31 screws were implanted in sheep hip bone for 3 and 6 months. The authors qualitatively showed the differences in the degradation behavior of the screws when comparing the screw threads, which were in contact with bone, and the screw head that was surrounded by the soft tissue on top of the bone.

The quantitative evaluation of degradation and osseointegration parameters such as the degradation rate, BIC, and BV/TV depends on the quality of image segmentation. This is hindered

**ADVANCED
SCIENCE NEWS**

www.advancedsciencenews.com

**ADVANCED
ENGINEERING
MATERIALS**

www.aem-journal.com

by similarities in grayscales between residual metal, degradation layer, and bone, due to similar X-ray attenuation coefficients of the materials and the presence of secondary phases in the degradation layer of some alloys.[148] A correlation between degradation rate, BIC and BV/TV, and implant stability can be obtained by conducting in situ pullout or pushout tests. Implant stability in this case refers to both the mechanical stability of the implant and its integration into the bone. Thus, crack formation in the bone and potentially the implant can be observed as a function of the applied force.[155–157] However, the resulting X-ray dose effected on the bone can change its mechanical properties,[158,159] thus the scanning speed must be optimized.

Following the completion of all 3D analyses, the explant can be cut in half along the implant's long axis, and thin section may be prepared for further measurements. The preparation of thin sections is technically difficult due to the differing mechanical properties of the bone and the metal; oftentimes the cut-and-grind method is used and recently it was shown that laser cutting also yields good results.[149] As a gold standard, histological analyses are conducted on thin sections following specific staining. It was shown that 3D and 2D calculations of degradation rate can differ strongly.[133,153] The 2D evaluation is error prone due to the strong dependence on the correct sectioning of the explant along a predefined cutting plane.

Below the microstructural level, which is accessible using SRμCT, lies the hierarchical level of bone, which consists of the lacuno-canalicular network (LCN) and bone lamellae. The LCN is of particular interest in bone research as the osteocytes, which reside in the lacunae, govern the bone remodeling process, i.e., the formation and removal of bone.[160,161] They are influenced by the shear stresses exerted on them due to the fluid flow in the LCN, arising, e.g., from loading of the bone. These stresses are converted into biochemical signals.[162,163] It was shown that osteocytes are influenced by the presence of implants, as they tend to align parallel to the implant surface of Ti implants and their density is increased.[164–166]

Canaliculi were shown to run both toward the implant surface and to connect to neighboring osteocytes and blood vessels.[165–167] The LCN was frequently analyzed using SRnCT to reveal its general morphology, in particular in the context of pathologies.[29,32,34,168–170] In addition to the LCN itself, SRnCT has been shown to enable the imaging of the collagen fiber orientation in the bone.[171] Utilizing highest resolution imaging has been found to be of particular importance to correctly determine the LCN morphology.[172] The influence of Mg alloy implants on the LCN morphology and function remains unexplored to date, but the chemical stimuli resulting from the material degradation are expected to influence the network organization.

At its lowest structural level bone consists of fibrils, which are a composite of type I collagen and hydroxyapatite crystal platelets (HAP),[173–175] the ultrastructure of bone. For the general overview on assessing bone ultrastructure, we refer the reader to a comprehensive review by Georgiadis et al.[176] SAXS and XRD can be used to determine the bone ultrastructure and degradation layer crystal composition, for example, in the form of scanning measurements on thin sections. HAP are structured in a hexagonal lattice, with $a = b = 0.94$ nm and $c = 0.68$ nm,[177] whose c-axis is aligned with the collagen fibers.[178,179] The platelets

can vary in size but measure $\approx 3 \times 25 \times 50$ nm.[174,180,181] Using high-resolution 2D scanning SAXS and XRD in combination with XRF, it was shown that higher concentrations of Mg were present around blood vessels and osteocyte lacunae for bone surrounding alloys ZX50 and WZ21. The presence of Mg was associated with a contraction of the HAP lattice.[182] Moreover, lower resolution SAXS measurements indicated that newly formed bone around WZ21 alloy displays a temporary decrease in platelet thickness at early healing times.[183] Both studies, however, lacked reference implants and a recent study using high-resolution SAXS and XRD suggested that platelet thickness in the implant vicinity does not differ significantly between Mg–xGd ($x = 5$ and 10 wt%) and Ti and PEEK implants or different time points.[149] Similarly, no differences were found for the degree of orientation of collagen fibrils. However, lattice spacing and crystal size of the (310)-reflection were shown to differ significantly for Mg–5Gd and Ti in particular. The same study suggested the presence of a hydroxyapatite in the degradation layer of the Mg–xGd implants, but with significant shift of crystal size and lattice spacing. However, due to a lack of data on element distribution, the observed differences could not be attributed to Mg or Gd. Recently, Liebi et al. published a preprint detailing the use of 6D SAXS to study the collagen orientation around ZX10 implants in 3D.[184] The technique can overcome limitations from imaging of thin sections, but long scanning times hinder the evaluation of a statistically significant number of samples.

5. Outlook and Conclusion

SR-based characterization techniques in Mg research have been used extensively to date in particular with respect to mechanical testing of Mg alloys to study the deformation modes and influence of alloying elements thereon using XRD. Moreover, the Mg microstructure, namely, the α-Mg dendrite growth, has been studied in detail using SRμCT during solidification. However, SR-based techniques have not been applied often in degradation testing and for ex vivo measurements. This may be due, in part, to the long preparation times associated with beamtime applications, during which the samples cannot be used for other characterization techniques. Moreover, while in situ measurements can provide insight into the processes occurring, e.g., during the implant degradation, the degradation speed of most Mg alloys is tailored to be so low that long imaging times are required to resolve the degradation using SRμCT. Thus, in situ SRnCT is expected to be used more frequently in the future, which requires the development of suitable sample cells, and for which small samples (≈ 100 μm) need to be manufactured. In addition, future experiments may make use of the unique capabilities of free electron lasers, to monitor events taking place at short time scales, such as the interaction between metal ions and organic molecules during Mg degradation. In addition to strengthening the understanding of certain mechanisms, in situ data also provide unique validation data for computational models. Moreover, tomographic images can be used as realistic input geometry for computational models. The increasing use of 3D in situ imaging also requires significant advances in automated image processing and segmentation to obtain meaningful results within a suitable time frame. To this end, developments in machine

learning, such as neural networks, for segmentation are critical. The trainable WEKA segmentation tool[185] available in Fiji/ImageJ[186] yields good results in many cases[137] and convolutional neural networks show promising results for more complex image data.[159]

Moreover, it is expected that future work will focus more strongly on the interaction of the material and biology, such as intracellular Mg and alloy element content during degradation, or cell adhesion on the degradation layer surface. Static SRμCT measurements based on attenuation contrast will likely be transferred to laboratory μCT machines, which can obtain similar resolutions. Moreover, the high-resolution image data can be registered to lower resolution in vivo image data, in which BIC and DR are often more difficult to ascertain. By performing this registration and determining a reliable correlation between quantitative values such as BIC, extracted from low- and high-resolution images, future SRμCT may be omitted.

Conflict of Interest

The authors declare no conflict of interest.

[1] W. J. Joost, P. E. Krajewski, *Scr. Mater.* **2017**, *128*, 107.

[2] F. Witte, *Acta Biomater.* **2010**, *6*, 1680.

[3] L. Ouyang, F. Liu, H. Wang, J. Liu, X. S. Yang, L. Sun, M. Zhu, *J. Alloys Compd.* **2020**, *832*, 154865.

[4] F. Feyerabend, J. Fischer, J. Holtz, F. Witte, R. Willumeit, H. Drucker, C. Vogt, N. Hort, *Acta Biomater.* **2010**, *6*, 1834.

[5] N. Hort, Y. Huang, D. Fechner, M. Stormer, C. Blawert, F. Witte, C. Vogt, H. Drucker, R. Willumeit, K. U. Kainer, F. Feyerabend, *Acta Biomater.* **2010**, *6*, 1714.

[6] M. M. Gawlik, B. Wiese, V. Desharnais, T. Ebel, R. Willumeit-Romer, *Materials* **2018**, *11*.

[7] M. Esmaily, J. E. Svensson, S. Fajardo, N. Birbilis, G. S. Frankel, S. Virtanen, R. Arrabal, S. Thomas, L. G. Johansson, *Prog. Mater. Sci.* **2017**, *89*, 92.

[8] S. Virtanen, *Mater. Sci. Eng.: B* **2011**, *176*, 1600.

[9] A. Myrissa, N. A. Agha, Y. Y. Lu, E. Martinelli, J. Eichler, G. Szakacs, C. Kleinhans, R. Willumeit-Romer, U. Schafer, A. M. Weinberg, *Mater. Sci. Eng.: C* **2016**, *61*, 865.

[10] J. Gonzalez, R. Q. Hou, E. P. S. Nidadavolu, R. Willumeit-Römer, F. Feyerabend, *Bioact. Mater.* **2018**, *3*, 174.

[11] P. K. Zysset, X. Edward Guo, C. Edward Hoffler, K. E. Moore, S. A. Goldstein, *J. Biomech.* **1999**, *32*, 1005.

[12] S. Hengsberger, A. Kulik, P. H. Zysset, *Bone* **2002**, *30*, 178.

[13] D. T. Reilly, A. H. Burstein, *J. Biomech.* **1975**, *8*, 393.

[14] M. J. Mirzaali, J. J. Schwiedrzik, S. Thaiwichai, J. P. Best, J. Michler, P. K. Zysset, U. Wolfram, *Bone* **2016**, *93*, 196.

[15] J. M. Seitz, A. Lucas, M. Kirschner, *JOM* **2016**, *68*, 1177.

[16] R. J. Werkhoven, W. H. Sillekens, J. B. J. M. van Lieshout, *Magnesium Technology*, John Wiley & Sons, Inc., Hoboken, NJ **2011**, p. 419.

[17] P. K. Bowen, E. R. Shearier, S. Zhao, R. J. Guillory, F. Zhao, J. Goldman, J. W. Drelich, *Adv. Healthc. Mater.* **2016**, *5*, 1121.

[18] J. Als-Nielsen, D. McMorrow, *Elements of Modern X-Ray Physics*, John Wiley & Sons **2011**, p. xii.

[19] *European Synchrotron Radiation Facility*, https://www.esrf.fr/home/UsersAndScience/Accelerators.html (accessed: May, 2021).

[20] *Deutsches Elektronensynchrotron DESY*, https://photon-science.desy.de/facilities/petra_iii/facility_information/index_eng.html (accessed: May, 2021).

[21] A. B. Excillium, https://www.excillum.com/products/metaljet/metaljet-d2-160-kv/ (accessed: May, 2021).

[22] E. Maire, P. J. Withers, *Int. Mater. Rev.* **2014**, *59*, 1.

[23] R. Mokso, F. Marone, D. Haberthür, J. C. Schittny, G. Mikuljan, A. Isenegger, M. Stampanoni, in *AIP Conf. Proc.*, American Institute of Physics AIP **2010**, p. 38.

[24] P. Cloetens, W. Ludwig, J. Baruchel, D. Van Dyck, J. Van Landuyt, J. P. Guigay, M. Schlenker, *Appl. Phys. Lett.* **1999**, *75*, 2912.

[25] J. Hagemann, M. Töpperwien, T. Salditt, *Appl. Phys. Lett.* **2018**, *113*, 041109.

[26] L. M. Lohse, A. L. Robisch, M. Töpperwien, S. Maretzke, M. Krenkel, J. Hagemann, T. Salditt, *J. Synchrotron Radiat.* **2020**, *27*, 852.

[27] C. Y. J. Hémonnot, S. Köster, *ACS Nano* **2017**, *11*, 8542.

[28] S. Flenner, M. Storm, A. Kubec, E. Longo, F. Doring, D. M. Pelt, C. David, M. Muller, I. Greving, *J. Synchrotron Radiat.* **2020**, *27*, 1339.

[29] M. Dierolf, A. Menzel, P. Thibault, P. Schneider, C. M. Kewish, R. Wepf, O. Bunk, F. Pfeiffer, *Nature* **2010**, *467*, 436.

[30] M. Langer, F. Peyrin, *Osteoporos. Int.* **2016**, *27*, 441.

[31] J. C. Andrews, E. Almeida, M. C. H. Van Der Meulen, J. S. Alwood, C. Lee, Y. Liu, J. Chen, F. Meirer, M. Feser, J. Gelb, J. Rudati, A. Tkachuk, W. Yun, P. Pianetta, *Microsc. Microanal.* **2010**, *16*, 327.

[32] A. Ciani, H. Toumi, S. Pallu, E. H. R. Tsai, A. Diaz, M. Guizar-Sicairos, M. Holler, E. Lespessailles, C. M. Kewish, *Bone Rep.* **2018**, *9*, 122.

[33] J. C. Andrews, S. Brennan, C. Patty, K. Luening, P. Pianetta, E. Almeida, M. C. H. van der Meulen, M. Feser, J. Gelb, J. Rudati, A. Tkachuk, W. B. Yun, *Synchrotron Radiat. News* **2008**, *21*, 17.

[34] M. Langer, A. Pacureanu, H. Suhonen, Q. Grimal, P. Cloetens, F. Peyrin, *PLoS One* **2012**, *7*, e35691.

[35] M. Töpperwien, A. Markus, F. Alves, T. Salditt, *Neuroimage* **2019**, *199*, 70.

[36] W. Ludwig, S. Schmidt, E. M. Lauridsen, H. F. Poulsen, *J. Appl. Crystallogr.* **2008**, *41*, 302.

[37] H. F. Poulsen, X. Fu, E. Knudsen, E. M. Lauridsen, L. Margulies, S. Schmidt, *Materials Science Forum*, Trans Tech Publications Ltd **2004**, p. 1363.

[38] F. Schaff, M. Bech, P. Zaslansky, C. Jud, M. Liebi, M. Guizar-Sicairos, F. Pfeiffer, *Nature* **2015**, *527*, 353.

[39] M. Liebi, M. Georgiadis, A. Menzel, P. Schneider, J. Kohlbrecher, O. Bunk, M. Guizar-Sicairos, *Nature* **2015**, *527*, 349.

[40] M. Georgiadis, M. Guizar-Sicarios, A. Zwahlen, A. J. Trüssel, O. Bunk, R. Müller, P. Schneider, *Acta Biomater.* **2015**, *71*, 42.

[41] E. Guo, S. Shuai, D. Kazantsev, S. Karagadde, A. B. Phillion, T. Jing, W. Li, P. D. Lee, *Acta Mater.* **2018**, *152*, 127.

[42] M. Y. Wang, J. J. Williams, L. Jiang, F. De Carlo, T. Jing, N. Chawla, *Scr. Mater.* **2011**, *65*, 855.

[43] M. Y. Wang, J. J. Williams, L. Jiang, F. De Carlo, T. Jing, N. Chawla, *Metallogr. Microstruct. Anal.* **2012**, *1*, 7.

[44] M. Y. Wang, Y. J. Xu, T. Jing, G. Y. Peng, Y. N. Fu, N. Chawla, *Scr. Mater.* **2012**, *67*, 629.

[45] M. Yang, S. M. Xiong, Z. Guo, *Acta Mater.* **2015**, *92*, 8.

[46] M. Yang, S. M. Xiong, Z. Guo, *Acta Mater.* **2016**, *112*, 261.

[47] S. Shuai, E. Guo, A. B. Phillion, M. D. Callaghan, T. Jing, P. D. Lee, *Acta Mater.* **2016**, *118*, 260.

[48] J. Du, Z. Guo, A. Zhang, M. Yang, M. Li, S. Xiong, *Sci. Rep.* **2017**, *7*, 1.

[49] S. Shuai, E. Guo, Q. Zheng, M. Wang, T. Jing, Y. Fu, *Mater. Charact.* **2016**, *118*, 304.

[50] S. Shuai, E. Guo, M. Wang, M. D. Callaghan, T. Jing, Q. Zheng, P. D. Lee, *Metall. Mater. Trans. A. Phys. Metall. Mater. Sci.* **2016**, *47*, 4368.

[51] E. Guo, A. B. Phillion, B. Cai, S. Shuai, D. Kazantsev, T. Jing, P. D. Lee, *Acta Mater.* **2017**, *123*, 373.

[52] S. Shuai, E. Guo, Q. Zheng, M. Wang, T. Jing, *Mater. Charact.* **2016**, *111*, 170.

[53] W. H. Sillekens, D. Casari, W. U. Mirihanage, S. Terzi, R. H. Mathiesen, L. Salvo, R. Daudin, P. Lhuissier, E. Guo, P. D. Lee, *JOM* **2016**, *68*, 3042.

[54] D. Tolnai, T. Sosro, S. Gavras, R. H. Buzolin, N. Hort, *Int. J. Mater. Res.* **2020**, *111*, 4.

[55] F. Witte, J. Fischer, F. Beckmann, M. Störmer, N. Hort, *Scr. Mater.* **2008**, *58*, 453.

[56] D. Tolnai, G. Requena, P. Cloetens, J. Lendvai, H. P. Degischer, *Mater. Sci. Eng.: A* **2012**, *550*, 214.

[57] G. Requena, P. Cloetens, W. Altendorfer, C. Poletti, D. Tolnai, F. Warchomicka, H. P. Degischer, *Scr. Mater.* **2009**, *61*, 760.

[58] C. Landron, E. Maire, J. Adrien, H. Suhonen, P. Cloetens, O. Bouaziz, *Scr. Mater.* **2012**, *66*, 1077.

[59] P. Barriobero-Vila, J. Gussone, J. Haubrich, S. Sandlobes, J. C. Da Silva, P. Cloetens, N. Schell, G. Requena, *Mater.* **2017**, *10*.

[60] B. Zeller-Plumhoff, A. L. Robisch, D. Pelliccia, E. Longo, H. Slominska, A. Hermann, M. Krenkel, M. Storm, Y. Estrin, R. Willumeit-Romer, T. Saldtt, D. Orlov, *Sci. Rep.* **2020**, *10*, 16101.

[61] D. Orlov, D. Pelliccia, X. Fang, L. Bourgeois, N. Kirby, A. Y. Nikulin, K. Ameyama, Y. Estrin, *Acta Mater.* **2014**, *72*, 110.

[62] J. J. Lombardo, R. A. Ristau, W. M. Harris, W. K. S. Chiu, *J. Synchrotron Radiat.* **2012**, *19*, 789.

[63] C. S. Kaira, C. Kantzos, J. J. Williams, V. De Andrade, F. De Carlo, N. Chawla, *Acta Mater.* **2018**, *144*, 419.

[64] P. Staron, T. Fischer, T. Lippmann, A. Stark, S. Daneshpour, D. Schnubel, E. Uhlmann, R. Gerstenberger, B. Camin, W. Reimers, E. Eidenberger, H. Clemens, N. Huber, A. Schreyer, *Adv. Eng. Mater.* **2011**, *13*, 658.

[65] A. Stark, M. Rackel, A. Tchouaha Tankoua, M. Oehring, N. Schell, L. Lottermoser, A. Schreyer, F. Pyczak, *Metals* **2015**, *5*, 2252.

[66] D. Tolnai, C. L. Mendis, A. Stark, G. Szakács, B. Wiese, K. U. Kainer, N. Hort, *Mater. Lett.* **2013**, *102–103*, 62.

[67] D. Tolnai, T. Subroto, S. Gavras, R. Buzolin, A. Stark, N. Schell, N. Hort, *Materials* **2018**, *11*.

[68] B. Wiese, C. L. Mendis, D. Tolnai, A. Stark, N. Schell, H. P. Reichel, R. Brückner, K. U. Kainer, N. Hort, *J. Alloys Compd.* **2015**, *618*, 64.

[69] J. Medina, P. Pérez, G. Garces, D. Tolnai, A. Stark, N. Schell, P. Adeva, *Mater. Charact.* **2016**, *118*, 186.

[70] B. Zhou, L. Wang, B. Chen, Y. Jia, W. Wen, D. Li, D. Shu, P. Jin, X. Zeng, W. Ding, *Mater. Sci. Eng.: A* **2017**, *708*, 319.

[71] D. M. Fronczek, R. Chulist, L. Litynska-Dobrzynska, S. Kac, N. Schell, Z. Kania, Z. Szulc, J. Wojewoda-Budka, *Mater. Des.* **2017**, *130*, 120.

[72] S. Biswas, H. G. Brokmeier, J. J. Fundenberger, S. Suwas, *Mater. Charact.* **2015**, *102*, 98.

[73] B. Hasse, M. Koçak, W. Reimers, *Mater. Sci. Forum* **2006**, *524–525*, 279.

[74] J. Hiscocks, B. J. Diak, A. P. Gerlich, M. R. Daymond, *Mater. Sci. Technol.* **2017**, *33*, 189.

[75] H. B. Yao, Y. Li, A. T. S. Wee, *Appl. Surf. Sci.* **2000**, *158*, 112.

[76] M. Wolff, T. Ebel, M. Dahms, *Adv. Eng. Mater.* **2010**, *12*, 829.

[77] E. P. S. Nidadavolu, D. Krüger, B. Zeller-Plumhoff, D. Tolnai, B. Wiese, F. Feyerabend, T. Ebel, R. Willumeit-Römer, *J. Magnes. Alloys* **2020**.

[78] B. Wang, K. Li, Y. Zhang, B. Yan, W. Lu, *Mod. Phys. Lett. B* **2013**.

[79] L. Li, L. Wang, J. Wang, H. Zhang, Q. Zhu, Z. Li, X. Zeng, *Metals* **2020**, *10*, 1198.

[80] K. D. Liss, K. Yan, *Mater. Sci. Eng.: A* **2010**, *528*, 11.

[81] K. D. Liss, K. Yan, M. Reid, *Mater. Sci. Eng.: A* **2014**, *601*, 78.

[82] L. Tan, X. Yu, P. Wan, K. Yang, *J. Mater. Sci. Technol.* **2013**, *29*, 503.

[83] M. Huppmann, S. Stark, W. Reimers, *Int. J. Mater. Res.* **2010**, *101*, 1441.

[84] S. B. Yi, H. G. Brokmeier, R. Bolmaro, K. U. Kainer, J. Homeyer, *Mater. Sci. Forum* **2005**, *495–497*, 1585.

[85] C. H. J. Davies, S. B. Yi, J. Bohlen, K. U. Kainer, H. G. Brokmeier, *Mater. Sci. Forum* **2005**, *495–497*, 1633.

[86] S. B. Yi, C. H. J. Davies, H. G. Brokmeier, R. E. Bolmaro, K. U. Kainer, J. Homeyer, *Acta Mater.* **2006**, *54*, 549.

[87] L. Lu, J. W. Huang, D. Fan, B. X. Bie, T. Sun, K. Fezzaa, X. L. Gong, S. N. Luo, *Acta Mater.* **2016**, *120*, 86.

[88] L. Wu, S. R. Agnew, Y. Ren, D. W. Brown, B. Clausen, G. M. Stoica, H. R. Wenk, P. K. Liaw, *Mater. Sci. Eng.: A* **2010**, *527*, 7057.

[89] N. B. Zhang, Y. Y. Zhang, S. Chen, B. B. Zhang, Z. L. Li, H. L. Xie, L. Lu, X. H. Yao, S. N. Luo, *Scr. Mater.* **2021**, *190*, 113.

[90] S. Kaboli, P. C. Burnley, *Mater. Sci. Eng.: A* **2019**, *739*, 99.

[91] G. Garcés, K. Máthis, P. Pérez, J. Čapek, P. Adeva, *Mater. Sci. Eng.: A* **2016**, *666*, 48.

[92] G. Garcés, E. Oñorbe, P. Pérez, I. A. Denks, P. Adeva, *Mater. Sci. Eng.: A* **2009**, *523*, 21.

[93] G. Garcés, E. Oñorbe, P. Pérez, M. Klaus, C. Genzel, P. Adeva, *Mater. Sci. Eng.: A* **2012**, *533*, 119.

[94] C. J. Hustedt, P. K. Lambert, V. Kannan, E. L. Huskins-Retzlaff, D. T. Casem, M. W. Tate, H. T. Philipp, A. R. Woll, P. Purohit, J. T. Weiss, S. M. Gruner, K. T. Ramesh, T. C. Hufnagel, *J. Dyn. Behav. Mater.* **2018**, *4*, 222.

[95] H. Zhang, A. Jérusalem, E. Salvati, C. Papadaki, K. S. Fong, X. Song, A. M. Korsunsky, *Int. J. Plast.* **2019**, *119*, 43.

[96] S. B. Yi, H. G. Brokmeier, R. E. Bolmaro, K. U. Kainer, T. Lippmann, *Scr. Mater.* **2004**, *51*, 455.

[97] C. C. Aydiner, J. V. Bernier, B. Clausen, U. Lienert, C. N. Tomé, D. W. Brown, *Phys. Rev. B* **2009**, *80*, 024113.

[98] L. Balogh, S. R. Niezgoda, A. K. Kanjarla, D. W. Brown, B. Clausen, W. Liu, C. N. Tomé, *Acta Mater.* **2013**, *61*, 3612.

[99] P. A. Lynch, M. Kunz, N. Tamura, M. R. Barnett, *Acta Mater.* **2014**, *78*, 203.

[100] M. Arul Kumar, B. Clausen, L. Capolungo, R. J. McCabe, W. Liu, J. Z. Tischler, C. N. Tomé, *Nat. Commun.* **2018**, *9*, 1.

[101] L. Li, *Trans. Nonferrous Met. Soc. China* **2015**, *25*, 2156.

[102] A. King, W. Ludwig, M. Herbig, J. Y. Buffire, A. A. Khan, N. Stevens, T. J. Marrow, *Acta Mater.* **2011**, *59*, 6761.

[103] T. J. Marrow, M. Mostafavi, T. Hashimoto, G. E. Thompson, *Int. J. Fatigue* **2014**, *66*, 183.

[104] B. Kondori, T. F. Morgeneyer, L. Helfen, A. A. Benzerga, *Acta Mater.* **2018**, *155*, 80.

[105] D. Steglich, T. F. Morgeneyer, *Int. J. Fract.* **2013**, *183*, 105.

[106] M. Lentz, M. Klaus, R. S. Coelho, N. Schaefer, F. Schmack, W. Reimers, B. Clausen, *Metall. Mater. Trans. A. Phys. Metall. Mater. Sci.* **2014**, *45*, 5721.

[107] M. Lentz, M. Klaus, M. Wagner, C. Fahrenson, I. J. Beyerlein, M. Zecevic, W. Reimers, M. Knezevic, *Mater. Sci. Eng.: A* **2015**, *628*, 396.

[108] Y. Kawamura, K. Hayashi, A. Inoue, T. Masumoto, *Mater. Trans.* **2001**, *42*, 1172.

[109] H. Okuda, T. Horiuchi, M. Yamasaki, Y. Kawamura, S. Kohara, *Scr. Mater.* **2014**, *75*, 66.

[110] G. Garcés, G. Requena, D. Tolnai, P. Pérez, J. Medina, A. Stark, N. Schell, P. Adeva, *Mater. Charact.* **2016**, *118*, 514.

[111] G. Garcés, G. Requena, D. Tolnai, P. Pérez, P. Adeva, A. Stark, N. Schell, *J. Mater. Sci.* **2014**, *49*, 2714.

[112] H. Okuda, M. Yamasaki, Y. Kawamura, M. Tabuchi, H. Kimizuka, *Sci. Rep.* **2015**, *5*, 14186.

[113] H. Okuda, H. Tanaka, T. Shiratake, M. Yamasaki, Y. Kawamura, *Acta Mater.* **2016**, *118*, 95.

[114] W. Y. Wang, B. Tang, S. L. Shang, J. Wang, S. Li, Y. Wang, J. Zhu, S. Wei, J. Wang, K. A. Darling, S. N. Mathaudhu, Y. Wang, Y. Ren, X. D. Hui, L. J. Kecskes, J. Li, Z. K. Liu, *Acta Mater.* **2019**, *170*, 231.

[115] H. Okuda, M. Yamasaki, Y. Kawamura, *Scr. Mater.* **2017**, *139*, 26.

[116] G. Garces, D. G. Morris, M. A. Muñoz-Morris, P. Perez, D. Tolnai, C. Mendis, A. Stark, H. K. Lim, S. Kim, N. Shell, P. Adeva, *Acta Mater.* **2015**, *94*, 78.

[117] K. Máthis, G. Garcés, K. Horváth, D. Drozdenko, P. Dobroň, *Miner. Met. Mater. Ser.* **2017**, 625.

[118] K. H. Fekete, D. Drozdenko, J. Čapek, K. Máthis, D. Tolnai, A. Stark, G. Garcés, P. Dobroň, *J. Magnes. Alloys* **2020**, *8*, 199.

[119] E. Oñorbe, G. Garcés, P. Pérez, S. Cabezas, M. Klaus, C. Genzel, E. Frutos, P. Adeva, *Scr. Mater.* **2011**, *65*, 719.

[120] J. Wang, L. Wang, G. Zhu, B. Zhou, T. Ying, X. Zhang, Q. Huang, Y. Shen, X. Zeng, H. Jiang, *Metall. Mater. Trans. A. Phys. Metall. Mater. Sci.* **2018**, *49*, 5382.

[121] D. Orlov, G. Raab, T. T. Lamark, M. Popov, Y. Estrin, *Acta Mater.* **2011**, *59*, 375.

[122] D. Orlov, K. D. Ralston, N. Birbilis, Y. Estrin, *Acta Mater.* **2011**, *59*, 6176.

[123] R. H. Buzolin, D. Tolnai, C. L. Mendis, A. Stark, N. Schell, H. Pinto, K. U. Kainer, N. Hort, *Mater. Sci. Eng.: A* **2015**, *640*, 129.

[124] R. H. Buzolin, C. L. Mendis, D. Tolnai, A. Stark, N. Schell, H. Pinto, K. U. Kainer, N. Hort, *Mater. Sci. Eng.: A* **2016**, *664*, 2.

[125] X. Zhou, C. Ha, S. Yi, J. Bohlen, N. Schell, Y. Chi, M. Zheng, H.-G. Brokmeier, *Metals* **2020**, *10*, 124.

[126] D. Tolnai, R. H. Buzolin, F. D'Elia, T. Subroto, S. Gavras, A. Stark, N. Schell, K. U. Kainer, N. Hort, *JOM* **2016**, *68*, 3051.

[127] D. Tolnai, M.-A. Dupont, S. Gavras, K. Fekete-Horváth, A. Stark, N. Schell, K. Máthis, *Materials* **2019**, *12*, 3935.

[128] S. Gavras, R. H. Buzolin, T. Subroto, A. Stark, D. Tolnai, *Materials* **2018**, *11*.

[129] P. A. Lynch, A. W. Stevenson, D. Liang, C. J. Bettles, *Mater. Sci. Eng.: A* **2012**, *550*, 1.

[130] M. Lentz, M. Klaus, W. Reimers, B. Clausen, *Mater. Sci. Eng.: A* **2013**, *586*, 178.

[131] E. Willbold, X. Gu, D. Albert, K. Kalla, K. Bobe, M. Brauneis, C. Janning, J. Nellesen, W. Czayka, W. Tillmann, Y. Zheng, F. Witte, *Acta Biomater.* **2015**, *11*, 554.

[132] F. W. Bach, M. Schaper, C. Jaschik, *Mater. Sci. Forum* **2003**, 1037.

[133] F. Witte, J. Fischer, J. Nellesen, C. Vogt, J. Vogt, T. Donath, F. Beckmann, *Acta Biomater.* **2010**, *6*, 1792.

[134] M. Lentz, M. Klaus, I. J. Beyerlein, M. Zecevic, W. Reimers, M. Knezevic, *Acta Mater.* **2015**, *86*, 254.

[135] A. J. Davenport, C. Padovani, B. J. Connolly, N. P. C. Stevens, T. A. W. Beale, A. Groso, M. Stampanoni, *Electrochem. Solid-State Lett.* **2007**, *10*, C5.

[136] F. Feyerabend, T. Dose, Y. Xu, F. Beckmann, M. Stekker, R. Willumeit-Römer, A. Schreyer, F. Wilde, J. U. Hammel, *SPIE Opt. Eng. + Appl.* **2016**, 99671X.

[137] B. Zeller-Plumhoff, H. Helmholz, F. Feyerabend, T. Dose, F. Wilde, A. Hipp, F. Beckmann, R. Willumeit-Römer, J. U. Hammel, *Mater. Corros.* **2018**, *69*, 298.

[138] E. P. S. Nidadavolu, F. Feyerabend, T. Ebel, R. Willumeit-Romer, M. Dahms, *Materials* **2016**, *9*.

[139] B. Zeller-Plumhoff, M. Gile, M. Priebe, H. Slominska, B. Boll, B. Wiese, T. Würger, R. Willumeit-Römer, R. H. Meißner, *Corros. Sci.* **2021**, *182*, 109272.

[140] J. D. Rodriguez-Blanco, S. Shaw, P. Bots, T. Roncal-Herrero, L. G. Benning, *J. Alloys Compd.* **2012**, S477.

[141] N. A. Agha, Z. Liu, F. Feyerabend, R. Willumeit-Römer, B. Gasharova, S. Heidrich, B. Mihailova, *Mater. Sci. Eng.: C* **2018**, *91*, 659.

[142] B. Zeller-Plumhoff, D. Laipple, H. Slominska, K. Iskhakova, E. Longo, A. Hermann, S. Flenner, I. Greving, M. Storm, R. Willumeit-Römer, *Bioact. Mater. Rev.* **2021**.

[143] A. Myrissa, S. Braeuer, E. Martinelli, R. Willumeit-Römer, W. Goessler, A. M. Weinberg, *Acta Biomater.* **2017**, *48*, 521.

[144] J. Ramalho, R. C. Semelka, M. Ramalho, R. H. Nunes, M. AlObaidy, M. Castillo, *AJNR Am. J. Neuroradiol.* **2016**, *37*, 1192.

[145] S. Lagomarsino, S. Iotti, G. Farruggia, A. Cedola, V. Trapani, M. Fratini, I. Bukreeva, A. Notargiacomo, L. Mastrototaro, C. Marraccini, A. Sorrentino, I. McNulty, S. Vogt, D. Legnini, S. Kim, A. Gianoncelli, J. A. M. Maier, F. I. Wolf, *Spectrochim. Acta* **2011**, *66*, 834.

[146] E. Malucelli, S. Iotti, A. Gianoncelli, M. Fratini, L. Merolle, A. Notargiacomo, C. Marraccini, A. Sargenti, C. Cappadone, G. Farruggia, I. Bukreeva, M. Lombardo, C. Trombini, J. A. Maier, S. Lagomarsino, *Anal. Chem.* **2014**, *86*, 5108.

[147] A. Procopio, E. Malucelli, A. Pacureanu, C. Cappadone, G. Farruggia, A. Sargenti, S. Castiglioni, D. Altamura, A. Sorrentino, C. Giannini, E. Pereiro, P. Cloetens, J. A. M. Maier, S. Iotti, *ACS Cent. Sci.* **2019**, *5*, 1449.

[148] S. Galli, J. U. Hammel, J. Herzen, T. Damm, R. Jimbo, F. Beckmann, A. Wennerberg, R. Willumeit-Römer, *SPIE Opt. Eng. + Appl.* **2017**, 996704.

[149] B. Zeller-Plumhoff, C. Malich, D. Kruger, G. Campbell, B. Wiese, S. Galli, A. Wennerberg, R. Willumeit-Romer, D. C. F. Wieland, *Acta Biomater.* **2020**, *101*, 637.

[150] E. A. Zimmermann, R. O. Ritchie, *Adv. Healthc. Mater.* **2015**, *4*, 1287.

[151] F. Witte, J. Fischer, J. Nellesen, H.-A. Crostack, V. Kaese, A. Pisch, F. Beckmann, H. Windhagen, *Biomaterials* **2006**, *27*, 1013.

[152] X. Guan, M. Xiong, F. Zeng, B. Xu, L. Yang, H. Guo, J. Niu, J. Zhang, C. Chen, J. Pei, H. Huang, G. Yuan, *ACS Appl. Mater. Interfaces* **2014**, *6*, 21525.

[153] S. Galli, *On Magnesium-Containing Implants for Bone Applications*, Faculty of Odontology, Malmö University **2016**.

[154] E. Willbold, A. A. Kaya, R. A. Kaya, F. Beckmann, F. Witte, *Mater. Sci. Eng.: B* **2011**, *176*, 1835.

[155] J. Moosmann, B. Zeller-Plumhoff, D. C. F. Wieland, S. Galli, D. Krüger, T. Dose, H. Burmester, F. Wilde, M. Bech, N. Peruzzi, B. Wiese, A. Hipp, F. Beckmann, J. Hammel, R. Willumeit-

Römer, *Dev. X-Ray Tomogr. XI*, International Society for Optics and Photonics **2017**.

[156] S. Le Cann, E. Tudisco, M. J. Turunen, A. Patera, R. Mokso, M. Tägil, O. Belfrage, S. A. Hall, H. Isaksson, *Front. Bioeng. Biotechnol.* **2019**, *6*, 208.

[157] S. Le Cann, E. Tudisco, M. Tägil, S. A. Hall, H. Isaksson, *Front. Bioeng. Biotechnol.* **2020**, *8*, 934.

[158] H. D. Barth, E. A. Zimmermann, E. Schaible, S. Y. Tang, T. Alliston, R. O. Ritchie, *Biomaterials* **2011**, *32*, 8892.

[159] J. Moosmann, D. C. F. Wieland, B. Zeller-Plumhoff, S. Galli, D. Krüger, A. Ershov, S. Lautner, J. Sartori, M. Dean, S. Köhring, H. Burmester, T. Dose, N. Peruzzi, A. Wennerberg, R. Willumeit-Römer, F. Wilde, P. Heuser, J. U. Hammel, F. Beckmann, *SPIE-Int. Soc. Opt. Eng.* **2019**, 41.

[160] L. F. Bonewald, *J Bone Min. Res* **2011**, *26*, 229.

[161] E. H. Burger, J. Klein-Nulend, *FASEB J.* **1999**, *13*, S101.

[162] K. Piekarski, M. Munro, *Nature* **1977**, *269*, 80.

[163] S. Weinbaum, S. C. Cowin, Y. Zeng, *J. Biomech.* **1994**, *27*, 339.

[164] F. A. Shah, A. Snis, A. Matic, P. Thomsen, A. Palmquist, *Acta Biomater.* **2016**, *30*, 357.

[165] F. A. Shah, P. Stenlund, A. Martinelli, P. Thomsen, A. Palmquist, *J. Mater. Sci. Mater. Med.* **2016**, *27*, 167.

[166] Z. Du, S. Ivanovski, S. M. Hamlet, J. Q. Feng, Y. Xiao, *Clin. Implant Dent. Relat. Res.* **2016**, *18*, 270.

[167] F. A. Shah, X. Wang, P. Thomsen, K. Grandfield, A. Palmquist, *ACS Biomater. Sci. Eng.* **2015**, *1*, 305.

[168] F. Peyrin, P. Dong, A. Pacureanu, M. Langer, *Curr. Osteoporos Rep.* **2014**, *12*, 465.

[169] B. Hesse, P. Varga, M. Langer, A. Pacureanu, S. Schrof, N. Männicke, H. Suhonen, P. Maurer, P. Cloetens, F. Peyrin, K. Raum, *J. Bone Min. Res.* **2015**, *30*, 346.

[170] P. Varga, B. Hesse, M. Langer, S. Schrof, N. Männicke, H. Suhonen, A. Pacureanu, D. Pahr, F. Peyrin, K. Raum, *Biomech. Model Mechanobiol.* **2015**, *14*, 267.

[171] P. Varga, A. Pacureanu, M. Langer, H. Suhonen, B. Hesse, Q. Grimal, P. Cloetens, K. Raum, F. Peyrin, *Acta Biomater.* **2013**, *9*, 8118.

[172] B. Yu, A. Pacureanu, C. Olivier, P. Cloetens, F. Peyrin, *Sci. Rep.* **2020**, *10*, 1.

[173] S. Weiner, H. D. Wagner, *Annu. Rev. Mater. Sci.* **1998**, *28*, 271.

[174] D. S. Bocciarelli, *Calcif. Tissue Res.* **1970**, *5*, 261.

[175] E. Beniash, *Wiley Interdiscip. Rev. Nanomed. Nanobiotechnol.* **2011**, *3*, 47.

[176] M. Georgiadis, R. Muller, P. Schneider, *J. R. Soc. Interface* **2016**, *13*.

[177] A. S. Posner, A. Perloff, A. F. Diorio, *Acta Crystallogr.* **1958**, *11*, 308.

[178] S. Rinnerthaler, P. Roschger, H. F. Jakob, A. Nader, K. Klaushofer, P. Fratzl, *Calcif. Tissue Int.* **1999**, *64*, 422.

[179] T. Nakano, K. Kaibara, Y. Tabata, N. Nagata, S. Enomoto, E. Marukawa, Y. Umakoshi, *Bone* **2002**, *31*, 479.

[180] R. A. Robinson, *J. Bone Jt. Surg. Am.* **1952**, *34-A*, 389.

[181] S. Weiner, W. Traub, *FASEB J* **1992**, *6*, 879.

[182] T. A. Grunewald, H. Rennhofer, B. Hesse, M. Burghammer, S. E. Stanzl-Tschegg, M. Cotte, J. F. Loffler, A. M. Weinberg, H. C. Lichtenegger, *Biomaterials* **2016**, *76*, 250.

[183] T. A. Grünewald, A. Ogier, J. Akbarzadeh, M. Meischel, H. Peterlik, S. Stanzl-Tschegg, J. F. Löffler, A. M. Weinberg, H. C. Lichtenegger, *Acta Biomater.* **2016**, *31*, 448.

[184] M. Liebi, V. Lutz-Bueno, M. Guizar-Sicairos, B. M. Schönbauer, J. Eichler, E. Martinelli, J. F. Löffler, A. Weinberg, H. Lichtenegger, T. A. Grünewald, *BioRxiv* **2020**.

[185] I. Arganda-Carreras, V. Kaynig, C. Rueden, K. W. Eliceiri, J. Schindelin, A. Cardona, H. Sebastian Seung, *Bioinformatics* **2017**, *33*, 2424.

[186] J. Schindelin, I. Arganda-Carreras, E. Frise, V. Kaynig, M. Longair, T. Pietzsch, S. Preibisch, C. Rueden, S. Saalfeld, B. Schmid, J. Y. Tinevez, D. J. White, V. Hartenstein, K. Eliceiri, P. Tomancak, A. Cardona, *Nat. Methods* **2012**, *9*, 676.

[187] I. Maskery, N. T. Aboulkhair, M. R. Corfield, C. Tuck, A. T. Clare, R. K. Leach, R. D. Wildman, I. A. Ashcroft, R. J. M. Hague, *Mater. Charact.* **2016**, *111*, 193.

[188] E. A. Zimmermann, E. Schaible, B. Gludovatz, F. N. Schmidt, C. Riedel, M. Krause, E. Vettorazzi, C. Acevedo, M. Hahn, K. Puschel, S. Tang, M. Amling, R. O. Ritchie, B. Busse, *Sci. Rep.* **2016**, *6*, 1.

[189] I. Marco, A. A. Myrissa, E. Martinelli, F. Feyerabend, R. Willumeit-Römer, A. M. Weinberg, O. Van der Biest, *ECM – ECells Mater. J.* **2017**.

Berit Zeller-Plumhoff is the Head of Department for Imaging and Data Science in the Institute of Metallic Biomaterials at Helmholtz-Zentrum Hereon. She received her Ph.D. degree in 2017 from the University of Southampton. Her current research interests focus on the multiscale in situ characterization of biodegradable magnesium alloys. She combines experimental data with computational modeling and methods from data science to attain a more comprehensive understanding of the degradation processes.